WILLIAM & MARY
CHARTERED 1693

2022

A Numerical Investigation of Hurricane Florence-Induced Compound Flooding in the Cape Fear Estuary Using a Dynamically Coupled Hydrological-Ocean Model

Daoyang Bao

Z. George Xue

John C. Warner

Melissa Moulton

Dongxiao Yin
Virginia Institute of Marine Science

See next page for additional authors

Follow this and additional works at: https://scholarworks.wm.edu/vimsarticles

Part of the Oceanography Commons

Recommended Citation

Authors

Daoyang Bao, Z. George Xue, John C. Warner, Melissa Moulton, Dongxiao Yin, and et al

Author Contributions:
Conceptualization: Z. George Xue, Melissa Moulton, Joseph B. Zambon, Ruoying He
Data curation: Christie A. Hegermiller
Formal analysis: Daoyang Bao
Funding acquisition: Z. George Xue, John C. Warner

A Numerical Investigation of Hurricane Florence-Induced Compound Flooding in the Cape Fear Estuary Using a Dynamically Coupled Hydrological-Ocean Model

Daoyang Bao[1], Z. George Xue[1,2,3] , John C. Warner[4] , Melissa Moulton[5], Dongxiao Yin[1,6] , Christie A. Hegermiller[4,7], Joseph B. Zambon[8] , and Ruoying He[8]

[1]Department of Oceanography and Coastal Sciences, Louisiana State University, Baton Rouge, LA, USA, [2]Center for Computation and Technology, Louisiana State University, Baton Rouge, LA, USA, [3]Coastal Studies Institute, Louisiana State University, Baton Rouge, LA, USA, [4]U.S. Geological Survey, Woods Hole Coastal and Marine Science Center, Woods Hole, MA, USA, [5]Climate and Global Dynamics Laboratory, National Center for Atmospheric Research, Boulder, CO, USA, [6]Now at Department of Physical Sciences, Virginia Institute of Marine Science, Gloucester Point, VA, USA, [7]Now at Sofar Ocean Technologies, San Francisco, CA, USA, [8]Department of Marine, Earth, and Atmospheric Sciences, North Carolina State University, Raleigh, NC, USA

Abstract Hurricane-induced compound flooding is a combined result of multiple processes, including overland runoff, precipitation, and storm surge. This study presents a dynamical coupling method applied at the boundary of a processes-based hydrological model (the hydrological modeling extension package of the Weather Research and Forecasting model) and the two-dimensional Regional Ocean Modeling System on the platform of the Coupled-Ocean-Atmosphere-Wave-Sediment Transport Modeling System. The coupled model was adapted to the Cape Fear River Basin and adjacent coastal ocean in North Carolina, United States, which suffered severe losses due to the compound flood induced by Hurricane Florence in 2018. The model's robustness was evaluated via comparison against observed water levels in the watershed, estuary, and along the coast. With a series of sensitivity experiments, the contributions from different processes to the water level variations in the estuary were untangled and quantified. Based on the temporal evolution of wind, water flux, water level, and water-level gradient, compound flooding in the estuary was categorized into four stages: (I) swelling, (II) local-wind-dominated, (III) transition, and (IV) overland-runoff-dominated. A nonlinear effect was identified between overland runoff and water level in the estuary, which indicated the estuary could serve as a buffer for surges from the ocean side by reducing the maximum surge height. Water budget analysis indicated that water in the estuary was flushed 10 times by overland runoff within 23 days after Florence's landfall.

Plain Language Summary Compound flooding refers to a phenomenon in which two or more flooding sources occur simultaneously or subsequently within a short period of time. In this study, we present a new numerical model that combines hydrological and ocean models to represent the exchange of water levels at the land-ocean interaction zone. To test the model's robustness, we use this model to simulate the water level changes in Cape Fear River Basin and adjacent coastal ocean in North Carolina, United States, for Hurricane Florence in 2018. The comparison between observed and simulated water level prove that the new model can better resolve the changes in water elevation during a hurricane event than the traditional method where the ocean model utilized the river model's outputs as its boundary condition. We further quantify the contributions from different processes to the water level variations in the estuary. The compound flooding in the estuary was categorized into four stages: (I) swelling, (II) local-wind-dominated, (III) transition and (IV) overland-runoff-dominated. The estuary could serve as a buffer for surges from the ocean side by reducing the maximum surge height. The water in the estuary was flushed 10 times by overland runoff within 23 days after Florence's landfall.

1. Introduction

Flooding is one of the most destructive natural disasters globally, having caused $1 trillion of economic damages and 220,000 deaths between 1980 and 2013 (Winsemius et al., 2016). Coastal regions are exposed to both fluvial and oceanic flood drivers, which, when combined, usually lead to compound flooding events (Moftakhari et al., 2017). The number of compound events in major coastal cities of the United States has significantly

Investigation: Daoyang Bao, Z. George Xue

Methodology: Daoyang Bao, Z. George Xue, Dongxiao Yin

Project Administration: Z. George Xue, John C. Warner

Resources: Z. George Xue, John C. Warner, Melissa Moulton

Software: Daoyang Bao, Dongxiao Yin

Supervision: Z. George Xue, John C. Warner

Validation: Daoyang Bao, Dongxiao Yin

Writing – original draft: Daoyang Bao, Z. George Xue

Writing – review & editing: Z. George Xue, John C. Warner, Melissa Moulton, Joseph B. Zambon

increased over the past century (Wahl et al., 2015). With a warming climate and rising sea level, the frequency of compound flooding events is likely to increase further in the future (Ghanbari et al., 2021), which, combined with the projected increase in coastal population (Bevacqua et al., 2020), highlights the need for appropriate simulation of compound flooding events.

The contribution of fluvial and oceanic processes to compound flooding events has been mainly investigated separately by hydrological and ocean models, respectively (Chen et al., 2021; Colby et al., 2001; Kumbier et al., 2018; Muñoz et al., 2020; Noh et al., 2019; Pasquier et al., 2019; Pietrafesa et al., 2019; Rego & Li, 2010). Numerical techniques are being developed in recent efforts to link two or more models to work simultaneously to account for the compound effects among different processes. These techniques can be grouped into two categories: linking (also known as one-way coupling) and coupling (Santiago-Collazo et al., 2019). Until now, most existing compound flooding models fall into the former category. In a linked model structure, the "main model" is responsible for simulating the compound flooding and other models provide necessary inputs, mostly as boundary conditions.

Linked models provide an accurate and efficient way to simulate the compound flooding in areas beyond the boundary of the "main model." However, because the linking technique only allows one-way data transmission between the two models, processes that occurred along the interface boundary cannot be captured. For example, the interface boundary of a linked hydrological model is usually set on the land side along the coastline, where ocean conditions (e.g., water level, flux, velocity) are passed to the hydrological model, yet no land-to-ocean discharge is included (Apollonio et al., 2020; Joyce et al., 2018; Yin et al., 2016). While ocean models can be extended inland with wetting and drying algorithms (e.g., Huang et al., 2021; Ye et al., 2020, 2021; Zhang et al., 2020), their upstream boundary is usually driven by streamflow (mostly point sources) from a hydrological model, thus the lateral inputs from adjacent land are not accounted for. In addition, the interface boundary between the hydrological model and ocean model needs to be placed far behind the landward limits of storm surges (Zhang et al., 2020), which can largely increase the computational domain of the ocean model and thus demands extra computing resources.

In contrast, two-way coupled models are ideal for compound flooding simulation as they can represent processes on both land and ocean sides and the interaction among them. Theoretically, the full equations included in ocean models can be simplified on the flood plains to achieve a more efficient computation and avoid numerical complexity (Perdikaris et al., 2018). Compared with the linked model approach, compound flooding studies using two-way coupled models are still very limited. Tang, Chien, et al. (2013), Tang, Kraatz, et al. (2013) coupled a shallow water model with the Finite Volume Coastal Ocean Model (FVCOM; Chen et al., 2003) to simulate small-scale nearshore processes (2D) and large-scale ocean circulation (3D) simultaneously. In this effort, nearshore processes were handled by shallow water equations, and ocean processes were governed by 3-D primitive equations. To achieve the two-way coupling, an overlapping area between the two models was designed where the water level and velocity computed by the two models are exchanged. Nevertheless, the shallow water model did not include hydrological processes such as precipitation and infiltration, and thus cannot accurately represent overland runoff. Cheng et al. (2010) coupled the 1-D Stream-River Network, 2-D Overland Regime, and 3-D Subsurface Media of the parallel WAterSHed Systems (pWASH123D; Cheng et al., 2007) with the Advanced Circulation Model (ADCIRC; Luettich et al., 1992) through the Earth System Modeling Framework (ESMF; Hill et al., 2004). There was no overlapping area in this model, instead, the two models communicated with each other through a shared boundary. Along this interface boundary, pWASH123D receives water level from ADCIRC and ADCIRC receives water flux from pWASH123D. The comparison between stand-alone, one-way, and two-way coupled experiments suggested that two-way coupling is necessary to reproduce the interaction between watershed and ocean. Nonetheless, their work mainly focused on demonstrating the coupling method and examining the consistency and computational cost of the coupled model. There was no model validation or hydrodynamic analysis from the coupled model results.

In this study, we present a novel method that not only exchanges key variables between the hydrological and ocean models but also incorporates a momentum flux between land and ocean processes. The dynamical coupling method was adapted to the boundaries of the hydrological modeling extension package of the Weather Research and Forecasting model (WRF-Hydro; Gochis et al., 2018) and that of the two-dimensional Regional Ocean Modeling System (ROMS 2D; Shchepetkin & McWilliams, 2005) on the platform of the Coupled Ocean-Atmosphere-Wave and Sediment Transport (COAWST) Modeling System (Warner et al., 2010). To test
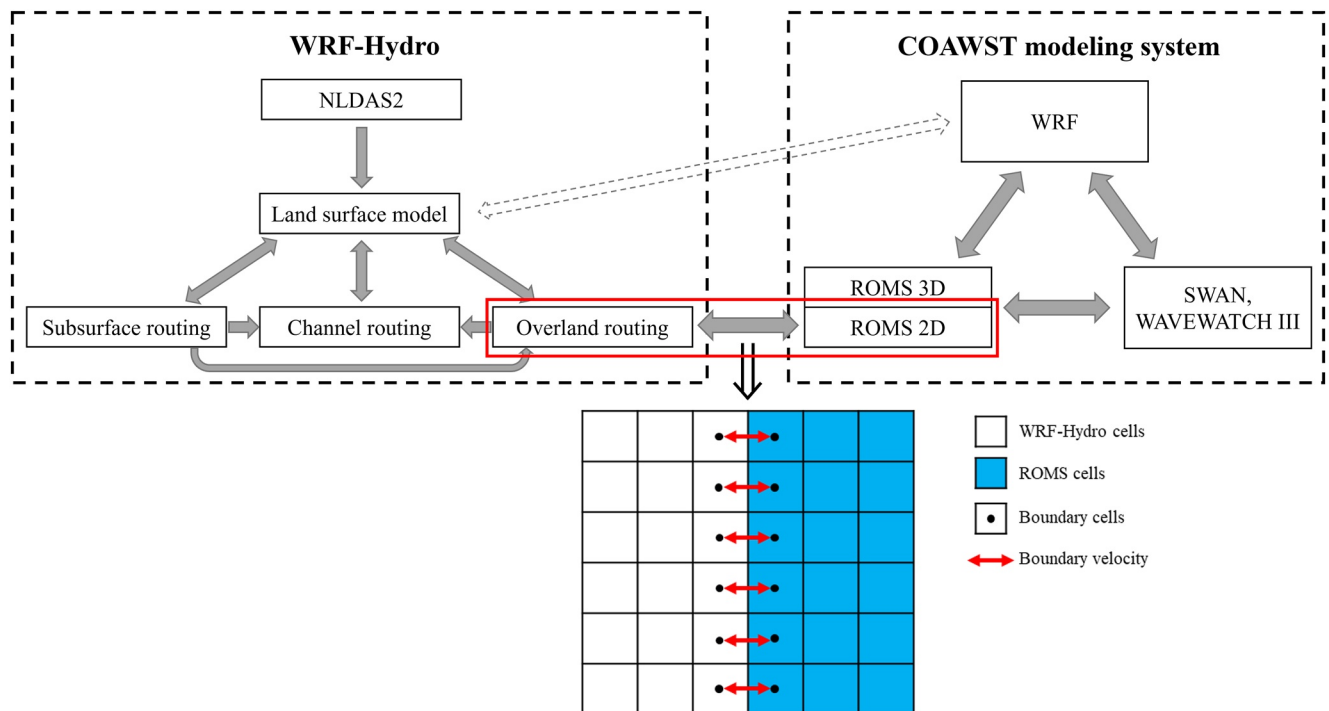
Figure 1. The framework of hydrological modeling extension package of the Weather Research and Forecasting model (WRF-Hydro) (upper left), Coupled-Ocean-Atmosphere-Wave-Sediment Transport (upper right), and schematic plot of the coupling between WRF-Hydro and two-dimensional Regional Ocean Modeling System model (lower). The red box is the work in this study. Two-headed arrows indicate two-way processes and single-headed arrows indicate one-way processes. The dashed arrow shows WRF-Hydro's capability of being two-way coupled with WRF, which is not included in this study.

the model's robustness, the coupled model was applied to the Cape Fear River Basin and adjacent coastal water for the extreme precipitation, storm surge, and resultant compound flooding forced by Hurricane Florence in 2018. By calculating the velocity on the interface boundary via differences in the water level between the two models, the coupled models achieved a transition on the interface boundary, and the model's capability to reproduce water level in the estuary is thus largely increased. The rest of the paper is organized as follows: details of the WRF-Hydro, ROMS 2D, and COAWST model, our novel dynamical coupling method, Hurricane Florence, and the Cape Fear Estuary are given in Section 2. Section 3 presents model validation. Section 4 focuses on the hydrodynamics and water budget in the Cape Fear River Estuary during and after Hurricane Florence. Section 5 discusses the nonlinear effects in the estuary between overland runoff and the residual water level from the ocean. Conclusions are given in Section 6.

2. Methods

2.1. WRF-Hydro

WRF-Hydro is a free, open-source, community-based, model-coupling framework designed to link multi-scale process models of the atmosphere and terrestrial hydrology (Gochis et al., 2018). It is an integrated system incorporating a land surface model (LSM), grid aggregation/disaggregation, subsurface flow routing, overland flow routing, and channel routing (Figure 1). WRF-Hydro has been successfully applied to simulate flooding events in different environment settings (e.g., Galanaki et al., 2021; Majidzadeh et al., 2017; Pal et al., 2021; Ryu et al., 2017; Wehbe et al., 2019). It also serves as the core of the National Ocean and Atmospheric Administration's National Water Model (NWM; https://water.noaa.gov/about/nwm) which provides streamflow forecasting over the entire continental United States.

For atmospheric forcing, WRF-Hydro can either be driven by external static data such as the Phase 2 of the North American Land Data Assimilation System (NLDAS2; https://ldas.gsfc.nasa.gov/nldas/v2/forcing) or can be coupled with meteorological and climate models such as the Weather Research and Forecasting Model (WRF,

Skamarock et al., 2021). Once rainfall reaches the land surface, the infiltration is first calculated by the LSM (e.g., the Noah LSM with multiparameterization options, Noah-MP; Niu et al., 2011). Selected model state and flux variables are then passed to/from the LSM grid to the terrain routing grid via a disaggregation/aggregation scheme. The subsurface lateral flow is calculated before routing the water to overland flow. The method used to calculate the lateral flow of saturated soil moisture was a quasi-three-dimensional flow representation by Wigmosta et al. (1994) and Wigmosta & Lettenmaier (1999). The rate of saturated subsurface flow from cell i, j to its down-gradient neighbors is calculated as:

$$q_{i,j} = \begin{cases} -T_{i,j}\, \beta_{i,j}\, w_{i,j} & \beta_{i,j} < 0 \\ 0 & \beta_{i,j} \geq 0 \end{cases} \tag{1}$$

in which $q_{i,j}$ is the flow rate from cell i, j, $T_{i,j}$ is the transmissivity at cell i, j, $\beta_{i,j}$ is the water table slope at cell i, j and $w_{i,j}$ is the width of cell i, j. $\beta_{i,j}$ is calculated as the difference in depths to the water table given by the LSM divided by the grid spacing. Transmissivity is calculated by a power law function:

$$T_{i,j} = \begin{cases} \dfrac{K\mathrm{sat}_{i,j}\, D_{i,j}}{n_{i,j}} \left(1 - \dfrac{z_{i,j}}{D_{i,j}}\right)^{n_{i,j}} & z_{i,j} \leq D_{i,j} \\ 0 & z_{i,j} > D_{i,j} \end{cases} \tag{2}$$

in which $K\mathrm{sat}_{i,j}$ is the saturated hydraulic conductivity, $n_{i,j}$ is the local power law exponent which is set to be 1 in the current version of WRF-Hydro, $D_{i,j}$ is the soil thickness at cell i, j and $z_{i,j}$ is the depth to water table at cell i, j given by the LSM.

Changes in depth to the water table are calculated as:

$$\Delta z_{i,j} = \frac{1}{\phi_{i,j}} \left(\frac{Q\mathrm{net}_{i,j}}{A_{i,j}} - R_{i,j} \right) \Delta t \tag{3}$$

in which $\phi_{i,j}$ is the soil porosity at cell i, j, $A_{i,j}$ is the grid cell area, $R_{i,j}$ is the soil column recharge rate from infiltration or deep subsurface injection, Δt is time step and $Q\mathrm{net}_{i,j}$ is the net saturated subsurface flow from cell i, j calculated by the sum of saturated subsurface flows from cell i, j in x-direction and y-direction. The depth to the water table $z_{i,j}$ was then changed by $\Delta z_{i,j}$. Negative values of $z_{i,j}$ represent the exfiltration of subsurface water to the surface which will be added to the infiltration excess (i_e in Equation 4) in overland routing. The overland flow was calculated whenever the depth of water on a model grid cell exceeds a specified retention depth. Once the overland flow enters a preset gridded channel network, channel flow will be calculated using an explicit, one-dimensional, variable time-stepping, diffusive wave formulation similar to that used in the overland flow calculation (Equations 4–6). For this study, we propose that, during a compound flooding event, the exchange of water between land and ocean should occur along the entire 0 m isobath instead of merely at the locations of the river mouth. Thus the channel routing was deactivated in the WRF-Hydro model.

The land-ocean coupling is realized by exchanging the water head data in the overland routing with ROMS 2D (red box in Figure 1). The overland routing is based on the diffusive wave approximation of the Saint-Venant equations (Equations 4–6), which assumes a balance between gravity and friction. It provides an accurate yet efficient way to compute the hydrodynamic movement of water in the watershed.

Continuity Equation:

$$\frac{\partial h}{\partial t} + \frac{\partial q_x}{\partial x} + \frac{\partial q_y}{\partial y} = i_e \tag{4}$$

Momentum Equations:

$$S_{fx} = S_{ox} - \frac{\partial h}{\partial x} \tag{5}$$

$$S_{fy} = S_{oy} - \frac{\partial h}{\partial y} \tag{6}$$

in which h is the surface flow depth, q_x, q_y are the unit discharge in x and y directions, t is time, i_e is the source term (infiltration excess), S_{fx}, S_{fy} are the friction slopes in x and y directions, and S_{ox}, S_{oy} are the bed slopes in x and y directions.

Manning's equation is used in solving the diffusive wave equations:

$$q = \alpha h^\beta, \ \alpha = S_f^{1/2}/n, \ \beta = 5/3 \tag{7}$$

in which q is the unit discharge, h is the surface flow depth, S_f is the friction slope, and n is the Manning roughness coefficient.

The computational domain of WRF-Hydro covers the entire watershed of interest. The water source in the overland routing is mainly the infiltration excess from the precipitation. Thus, the lateral boundary conditions for a closed basin are set as a gradient boundary condition:

$$\frac{\partial q_x}{\partial x} = 0 \tag{8}$$

$$\frac{\partial q_y}{\partial y} = 0 \tag{9}$$

2.2. ROMS 2D

ROMS is a free-surface, terrain-following, primitive equations ocean model that has been adapted to simulate water level and storm surge during various hurricane events (e.g., Li et al., 2006; Miles et al., 2017; Olabarrieta et al., 2012; Steffen & Bourassa, 2020; Zambon et al., 2014a, 2014b, 2021; Zang et al., 2018). ROMS uses structured quadrilateral grids (finite difference), which have higher numerical accuracy and computational efficiency than unstructured grids (Ding et al., 2021). ROMS also provides interfaces to exchange data with other models such as the Simulating WAves Nearshore (SWAN; Booij et al., 1999) and WRF on the platform of COAWST (Warner et al., 2010; Figure 1). Within COAWST, different models can perform two-way data exchange at user-configurable intervals via the model coupling toolkit (MCT; Jacob et al., 2005). The spherical coordinate remapping interpolation package (SCRIP; Jones, 1998) is used to compute interpolation weights to allow data exchange between different model grids.

ROMS supports both 2D and 3D simulation. In this study, WRF-Hydro is coupled with ROMS 2D (Figure 1). The equations of motion used in the ROMS 2D are given as:

Continuity Equation:

$$\frac{\partial \eta}{\partial t} + \frac{\partial \overline{u}D}{\partial x} + \frac{\partial \overline{v}D}{\partial y} = 0 \tag{10}$$

Momentum Equations:

$$\frac{\partial \overline{u}D}{\partial t} + \frac{\partial \overline{u}^2 D}{\partial x} + \frac{\partial \overline{uv}D}{\partial y} - f\overline{v}D = -gD\frac{\partial \eta}{\partial x} + \frac{\tau_{sx} - \tau_{bx}}{\rho D} + G_x \tag{11}$$

$$\frac{\partial \overline{v}D}{\partial t} + \frac{\partial \overline{uv}D}{\partial x} + \frac{\partial \overline{v}^2 D}{\partial y} + f\overline{u}D = -gD\frac{\partial \eta}{\partial y} + \frac{\tau_{sy} - \tau_{by}}{\rho D} + G_y \tag{12}$$

in which $\overline{u}$ and $\overline{v}$ are depth-averaged velocities in x and y directions, t is time, f is Coriolis parameter, ρ is water density, D is water depth, η is surface elevation, g is the gravitational acceleration, τ_{sx} and τ_{sy} are the surface wind stresses, τ_{bx} and τ_{by} are the bottom stresses, and G_x and G_y are the diffusive terms.

τ_{sx} and τ_{sy} are calculated as:

$$\tau_{sx} = \rho_{air} C_{Ds} u_{10}|\boldsymbol{U}_{10}| \tag{13}$$

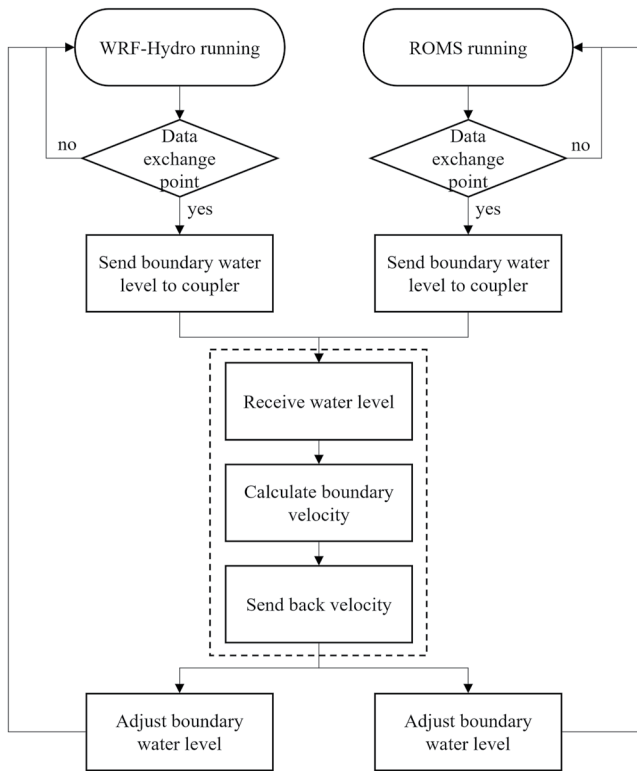$$\tau_{sy} = \rho_{air} C_{Ds} v_{10}|\boldsymbol{U}_{10}| \tag{14}$$

Figure 2. Flow chart of the dynamical coupling routing. Processes in the dashed box are done in the coupler (MCT).

$$C_{Ds} = \begin{cases} 1.15 \times 10^{-3} & |U_{10}| < 10.15 \\ 4.9 \times 10^{-4} + 6.5 \times 10^{-5} \times |U_{10}| & |U_{10}| \geq 10.15 \end{cases} \tag{15}$$

in which ρ_{air} is air density which is set to be 1.22 kg/m^2 in ROMS 2D, u_{10} and v_{10} are the wind speeds at 10 m above the sea surface in x and y directions, U_{10} is the wind vector at 10 m above the sea surface and C_{Ds} is the drag coefficient for wind stress.

τ_{bx} and τ_{by} are calculated as:

$$\tau_{bx} = \rho C_{Db} \bar{u} |\overline{U}| \tag{16}$$

$$\tau_{by} = \rho C_{Db} \bar{v} |\overline{U}| \tag{17}$$

in which $\overline{U}$ is depth-averaged velocity vector and C_{Db} is the drag coefficient for bottom stress specified by the user.

The open boundary conditions for ROMS 2D can be prescribed using either observed data or outputs from other models with user-specific options (please see Section 2.4 for details of the prescription of the ROMS 2D for the open ocean side).

2.3. Coupling Between WRF-Hydro and ROMS 2D

The coupled model in this study is built on COAWST, which already hosts the ROMS model. We adapted WRF-Hydro to COAWST using the model coupler (MCT) therein to enable the data exchange (Figure 1). Since both of WRF-Hydro and ROMS use a structured quadrilateral grid, the two models can share the same domain to simplify the coupling and at the same time avoid remapping and interpolation on the interface boundary. In this study, WRF-Hydro and ROMS 2D share the same domain, with an interface boundary to connect the two models (the land mask of the ROMS 2D model is the computation model of WRF-Hydro, and vice versa). Along this boundary, the two models exchange water level information on every connected cell. Mass conservation is guaranteed by using the coupler (MCT) to assure the two models have the same flux along the interface boundary. Specifically, the two models first send the calculated water level to the coupler, where the depth-averaged velocity is calculated. Then the coupler sends the boundary velocity back to the two models to ensure a consistent mass flux on their boundaries, respectively (Figure 2). On the interface boundary, a reduced physics approximation is applied to calculate the boundary velocity. The reduced physics momentum equations include a local acceleration term, a pressure gradient term, and a friction term (Equations 18 and 19). This provides a stable transition between the different physics used by the two models.

$$\frac{\partial \bar{u}_i}{\partial t} = -g \frac{\partial \eta}{\partial x} + \frac{\tau_{bx}}{\rho D} \tag{18}$$

$$\frac{\partial \bar{v}_i}{\partial t} = -g \frac{\partial \eta}{\partial y} + \frac{\tau_{by}}{\rho D} \tag{19}$$

in which, $\bar{u}_i$ and $\bar{v}_i$ are depth-averaged velocities along the interface boundary(red arrows in Figure 1), t is time, ρ is water density, D is water depth, η is surface elevation, g is the gravitational acceleration and τ_{bx}, τ_{by} are the bottom stresses in x and y directions calculated as Equations 16 and 17.

Once the boundary velocities are calculated, they are sent back to the two models as clamped boundary conditions:

$$q = \bar{u}_i D \tag{20}$$
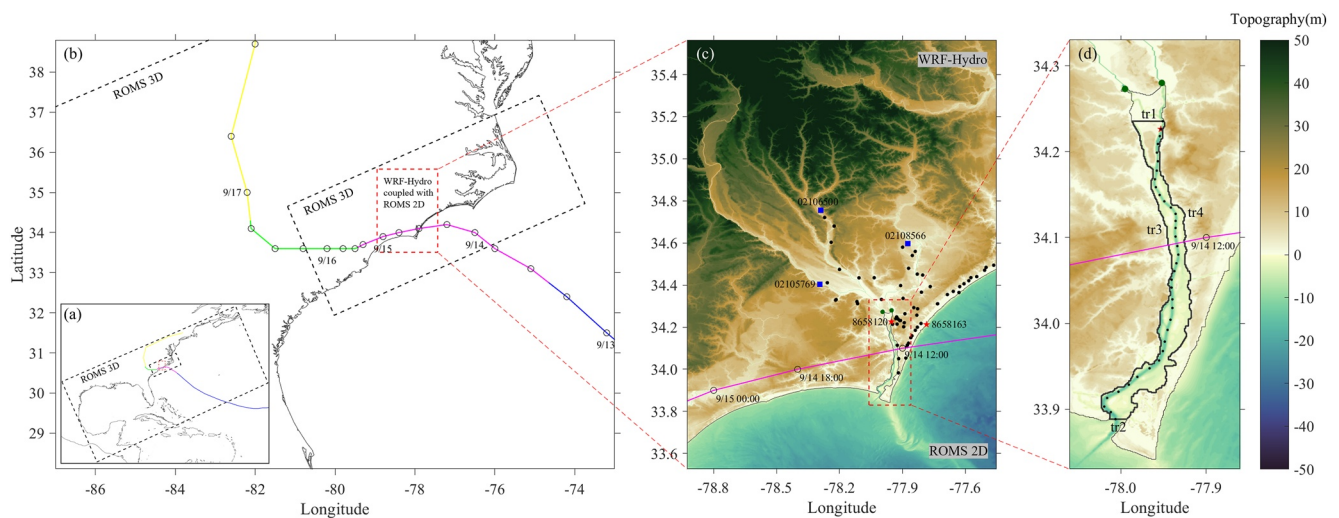
$$\bar{u} = \bar{u}_i \tag{21}$$

Figure 3. Maps of study area and model domains. (a) Black dashed boxes represent "parent" ROMS 3D domains; red dashed box represents coupled model domain; the colored line represents the track of Hurricane Florence in four stages: (I) swelling (blue), (II) local-wind-dominated (magenta), (III) transition (green), and (IV) overland-runoff-dominated (yellow). (b) Zoom-in view of 1-km Carolina domain and coupled model domain; colored line with circles represents the track of Hurricane Florence with a 6-hr interval in four stages. (c) Coupled model domain shared by two-dimensional Regional Ocean Modeling System (ROMS 2D) and WRF-Hydro. Red stars represent NOAA water level stations; blue squares represent USGS gages; black dots represent locations where USGS high water marks are available; the gray line represents interface boundary between two models; green dots represent point sources from National Water Model (NWM) for the linked ROMS 2D experiment. (d) The Cape Fear River Estuary. Bold lines (tr1 through tr4) represent transects for flux analysis; black dots represent sample points along the channel; green dots represent point sources from NWM for the linked ROMS 2D experiment.

In which, q is the unit discharge on the interface boundary in WRF-Hydro and $\bar{u}$ is the depth-averaged velocity on the interface boundary in ROMS 2D.

2.4. Hurricane Florence and Model Setup

Hurricane Florence (2018) was the sixth hurricane and the first major hurricane of the 2018 Atlantic hurricane season. Hurricane Florence originated from the west coast of Africa on 30 August, then moved across the Atlantic Ocean and made landfall near Wrightsville Beach, North Carolina on 14 September. After landfall, Florence moved westward at a slow speed. On 16 September, Florence made a northward turn in South Carolina then passed over North Carolina, Tennessee, and Virginia, and finally dissipated over Massachusetts on 18 September. Due to its slow motion and the "L-shaped" path, Florence introduced huge precipitation in the Cape Fear River Basin and set new records of peak flows in most of the channels and tributaries therein (Stewart & Berg, 2019; Yin et al., 2021). On the ocean side, Florence generated a huge storm surge, and the inundation heights along the North Carolina coast reached 2.5–3.4 m (8–11 ft) (Stewart & Berg, 2019). In this study, we focus on the water level development regarding the evolution of Florence in the Cape Fear River Estuary as estuaries usually have remarkable responses to a hurricane event (Cho et al., 2012; Du et al., 2019; Valle-Levinson et al., 2020).

In the coupled model, WRF-Hydro and ROMS 2D share the same domain covering the Florence landfall area (red dashed box in Figures 3a and 3b). The domain has a 100-m horizontal grid spacing and covers the entire lower Cape Fear River Basin, Cape Fear River Estuary, and adjacent coastal regions (Figure 3c). The domain was divided into two subdomains, one for WRF-Hydro and the other for ROMS 2D, bounded by the 0-m isobath referenced to NAVD88 (gray line in Figures 3c and 3d). The topography used in WRF-Hydro was derived from the National Hydrography Data set Plus Version 2 (NHDPlusV2; https://nhdplus.com/NHDPlus/NHDPlusV2_home.php). Since NHDPlusV2 data does not include channel depths, the major channels (stream order >3) were manually set to 10 m deep. In this study, the channel routing was disabled because the channel routing scheme in WRF-Hydro does not incorporate overbank flooding, which could lead to an unrealistically high water level when a large amount of water flows in from the adjacent land surface. WRF-Hydro was driven by hourly forcing data (including precipitation, air temperature, wind, short and long wave radiation, humidity, and pressure) regridded from NLDAS2. More details of this WRF-Hydro setup can be found in Yin et al. (2022).

Table 1
Experimental Design

Name	Coupling method	Precipitation in WRF-Hydro	Wind in ROMS
Exp1	Stand-alone ROMS 2D	–	Yes
Exp2	Linked ROMS 2D	Yes (as discharge provided from NWM)	Yes
Exp3	Dynamical coupling	Yes	Yes
Exp4	Dynamical coupling	Yes	No
Exp5	Dynamical coupling	No	Yes
Exp6	Dynamical coupling	No	No

Note. WRF-Hydro, hydrological modeling extension package of the Weather Research and Forecasting model; ROMS, Regional Ocean Modeling System; NWM, National Water Model.

Along the land-ocean boundary, ROMS 2D receives boundary conditions provided by a "parent" ROMS 3D model covering the Carolina coast (1 km horizontal grid spacing, Figure 3b). The Carolina model was nested in another ROMS 3D model covering the entire US east coast (4 km horizontal grid spacing, Figure 3a; Warner et al., 2010). The water level (zeta) calculated by the Carolina model was interpolated to the open boundary of ROMS 2D as the Chapman boundary condition (Chapman, 1985). The depth-averaged velocity results (ubar, vbar) from the Carolina model were interpolated to the open boundary of ROMS 2D as the Flather boundary condition (Flather, 1987). The bathymetry in the ROMS 2D model combines the Coastal Relief Model in the open ocean (https://www.ngdc.noaa.gov/mgg/coastal/crm.html) and NCEI Estuarine Bathymetric Digital Elevation Models in the Cape Fear River Estuary (https://www.ngdc.noaa.gov/mgg/bathymetry/estuarine). The tidal forcing was derived from the TPXO tidal solutions (Egbert & Erofeeva, 2002; https://www.tpxo.net), and the atmospheric forcing (10-m wind, rain rate, longwave and shortwave radiation, surface air pressure, temperature, and humidity) was derived from the Rapid Refresh atmospheric analysis (RAP; Benjamin et al., 2016; https://www.ncei.noaa.gov/data/rapid-refresh/access/historical/analysis). The bottom drag coefficient C_{Db} was set to 3×10^{-3} based on model calibration by fitting the observed water level data at NOAA stations Wrightsville Beach and Wilmington. The time steps of the WRF-Hydro and ROMS 2D were set to 1 and 3 s, respectively. The time interval of the coupling of the two models was set to 3 s. The model was initialized on 8 September 2018 0:00 and iterated for 30 days. The 30-day simulation took ~6.6 hr using 480 cores on LSU's QB3 cluster (http://www.hpc.lsu.edu/resources/hpc/system.php?system=QB3).

2.5. Experiment Design

To assess the potential advantages of a dynamical coupling approach, the experimental design was configured with increasing level of complexity (Table 1). First we setup a stand-alone ROMS 2D (Exp1) in which no river input was prescribed. Second, a linked ROMS 2D experiment (Exp2) was performed in which the streamflow discharge was provided from the NWM (https://water.noaa.gov) and prescribed as two point-sources in the estuary head (green dots in Figures 3c and 3d).

Exp3 is the control run using the dynamical coupling method. First, we tested if the coupled model's performance is superior to that of the stand-alone ROMS 2D and linked ROMS 2D setup (Exp1 and Exp2, details see Section 3). Then, another three sensitivity experiments were carried out to quantify the contribution from different processes to water level variations in the estuary: Exp4 and Exp5 were designed to assess the individual impact of wind and precipitation, respectively. For Exp4, the wind stress was switched off in all ROMS setups so there was no local wind or swell propagating into the ocean model from the "parent" ocean domains. For Exp5, the precipitation forcing in WRF-Hydro was set to zero, thus there was no overland runoff. In Exp6, both wind and precipitation were switched off. Therefore, the difference in model simulated water level between Exp3 and that from Exp4, Exp5, and Exp6 can be treated as the contribution from overland runoff, ocean processes (mainly from wind), and compound effects, respectively.
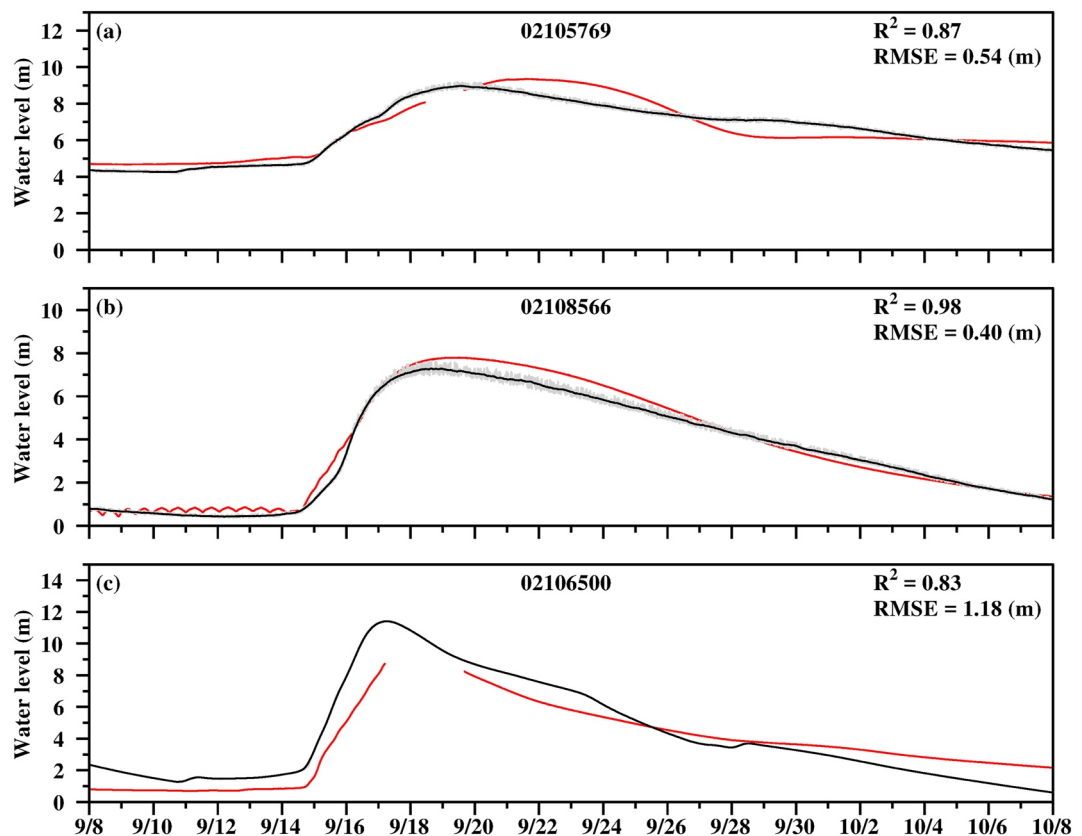
Figure 4. Comparison of water level between observed data (red), raw model outputs (gray) and model outputs smoothed through a Savitzky Golay filter (black) at three USGS gages.

3. Model Validation

We compared model simulated water level against available observations in the Cape Fear River Basin, Cape Fear River Estuary, and coastal regions to assess the performance of the coupled model.

3.1. Channel Water Level

There are three USGS gages, one located in each of the three main tributaries that discharge into the Cape Fear River Estuary. Station 02105769 is on the main stem of the Cape Fear River, 02108566 is on the Northeast Cape Fear River, and 02106500 is on the Black River (https://dashboard.waterdata.usgs.gov, blue squares in Figure 3c). In Figure 4, we compare model simulated water level against the records at the three gages. A Savitzky Golay filter is applied to eliminate the noises caused by numerical oscillations. The noises are more salient at gages 02105769 and 02108566 than gage 02106500 (overlapped with smoothed time series in Figure 4c). The smoothed water level time series show good agreement with the gage record with a coefficient of determination (R^2) value higher than 0.80 at all three stations. We notice that model-simulated streamflow peaks are ahead of the observed peaks at the three stations which can be caused by the uncertainties from precipitation forcing (Yin et al., 2021). The model underestimates peak level in the main stem of the Cape Fear River (02105769) and the Northeast Cape Fear River (02108566) while overestimating the peak level in the Black River (02106500). The mean absolute root mean square error (RMSE) are 0.54, 0.40, and 1.18 m at gages 02105769, 02108566, and 02106500, which are 5.8%, 5.1%, and 10.3% of the water level peak, respectively.

3.2. High Water Mark

The high water mark (HWM) refers to the highest level the water can reach during a flood event. Figure 5a shows the model-simulated highest water head by WRF-Hydro and highest water level in ROMS 2D during the
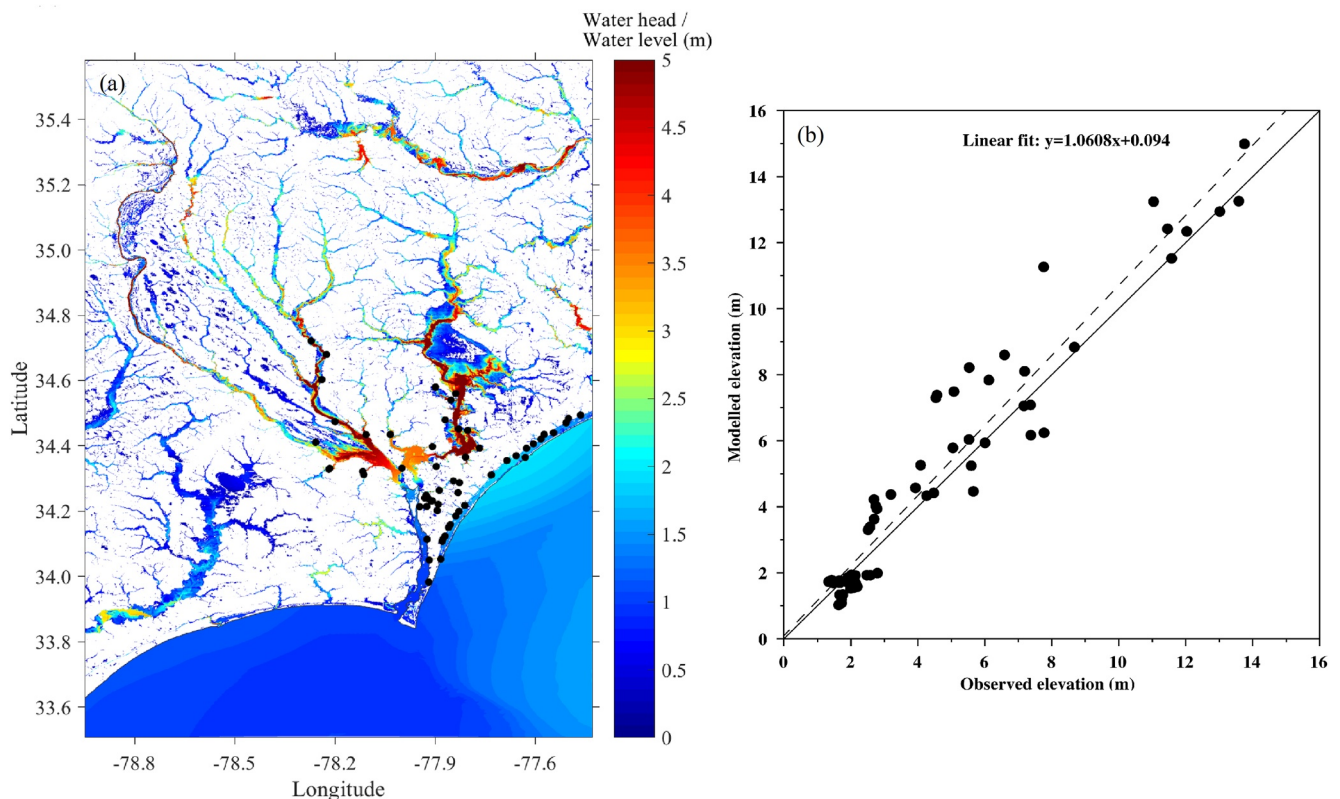
Figure 5. Comparison between observed and model-simulated high water marks (HWMs). (a) Modeled highest water head in hydrological modeling extension package of the Weather Research and Forecasting model and highest water level in Regional Ocean Modeling System during Florence. (b) Regression between the observed and modeled elevation of HWMs.

simulation period. The map demonstrates that the coupled model provided an integrated land-to-ocean simulation of a hurricane-induced compound event. The dynamical coupling method ensures the smoothing transition on the interface boundary.

The HWMs recorded by USGS are identified by the physical evidence remaining after the flood events, and usually have an uncertainty of ±0.02–0.12 m (Koenig et al., 2016). The HWM records were downloaded from https://stn.wim.usgs.gov/FEV/#FlorenceSep2018, for 63 sites covering the region downstream of the three USGS gages and the coast to the east of the Cape Fear River Estuary (black dots in Figures 3c and 5a). Figure 5b shows the correlation between observed and modeled HWMs with a slope close to 1, indicating that the model can reproduce both the magnitude and spatial distribution of water elevation peaks reasonably well.

3.3. Water Level in the Estuary and Coastal Region

Water level data at two NOAA stations (red stars in Figure 3c) were retrieved (https://tidesandcurrents.noaa.gov/stations.html?type=Water+Levels) to evaluate the model's performance in the estuary and coastal ocean. The Wrightsville Beach station (8658163) is located along the coastal line facing the open ocean and thus can represent oceanic processes such as tides and storm surges. The Wilmington station (8658120) is located at the head of the Cape Fear River Estuary and is a good index for the compound effect from fluvial and oceanic processes.

A comparison of the time series of observed water level and that simulated from the stand-alone (Exp1), linked (Exp2), and coupled model (Exp3) is shown in Figure 6. At the coastal station Wrightsville Beach, three model results overlap with each other. The models performed well in reproducing the magnitude and temporal variation of water level (R^2 = 0.81 and RMSE are 0.22 m for all experiments). No salient difference is identified among the time series of the three experiments. In contrast, at the head of the estuary (Wilmington station), the coupled model outperforms the stand-alone and linked models, better simulating the elevated water level and reduced tidal
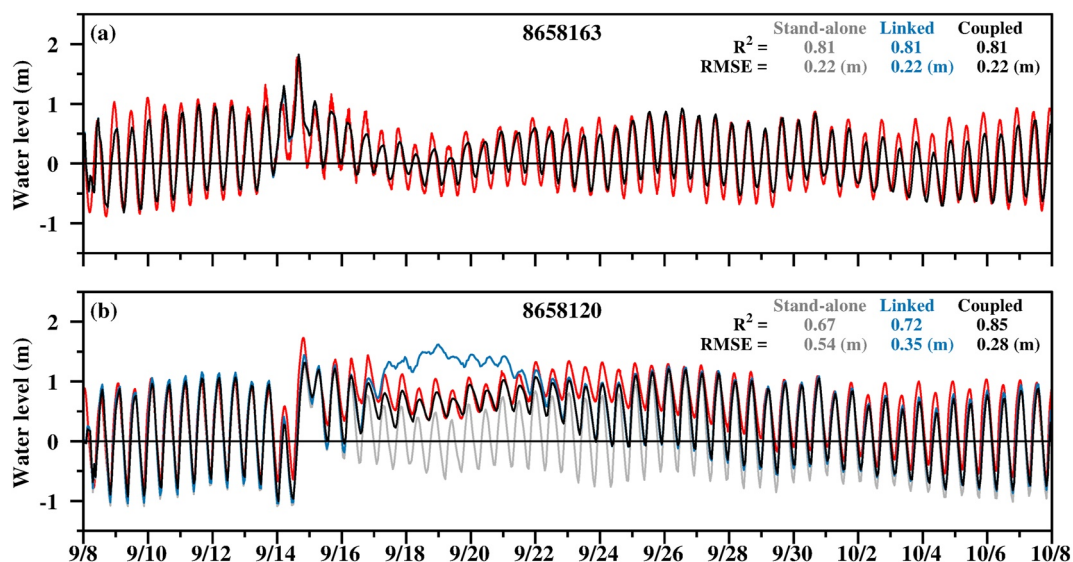
Figure 6. Comparison of water level between observed data (red), stand-alone model results (gray, Exp1), linked model results (blue, Exp2) and coupled model results (black, Exp3) at two NOAA stations.

variations during the post-hurricane period (after Sept 16th, 2018). The water level simulated by the stand-alone model drops rapidly after the landfall of Florence because of the retreat of surge water. In contrast, the linked model overestimates the water level by 0.5–1.0 m in the same period. Ye et al. (2021) reported an overestimate of NWM discharge compared with observed data in the Cape Rear River Basin after the landfall of Florence (the peak of NWM discharge was about twice of observed peak). For the coupled model (Exp3), the results exhibit a 0.3–1.0 m (approximately 20%–40%) improvement in reproducing observed water levels compared with the other two experiments. Coefficients of determination (R^2) of the coupled model are 0.18 and 0.13 higher than that of the stand-alone model and linked model, respectively. The RMSE of the coupled model is 0.26 and 0.07 m lower than that of the stand-alone model and linked model, respectively. These results confirmed the superior performance of the coupled model and all results presented in the following sections are based on the four experiments where the dynamical coupling approach is applied (Exp3 through Exp6).

4. Results

4.1. Development of Hurricane Florence

The Cape Fear River Estuary was exposed to different forcings during the development of Hurricane Florence. Before Florence made landfall, the water level in the estuary was mainly influenced by strong wind forcing. The wind effect can be divided into local and remote contributions, both of which can generate water level fluctuations in the estuary, with an additional surface slope that can be induced by local winds (Garvine, 1985). After Florence made landfall, the estuary was dominated by huge runoff from precipitation. A surface slope along the estuary can be induced by inputs from the overland runoff (Cai et al., 2014).

To illustrate the impact of Hurricane Florence as it developed, the time series of wind vectors, the water level at the estuary head and the mouth, their difference, as well as the flux at these two sites are plotted in Figure 7. The results are filtered with a moving average window of 12 hr and Exp6 are subtracted from other experiments to remove the tidal contribution to water levels and fluxes. The compound flooding event is categorized into four stages, which are (I) swelling, (II) local-wind-dominated, (III) transition, and (IV) overland-runoff-dominated. Five time points were chosen to illustrate the representative water level setup for each stage (arrows in Figure 7f, one for Stage I [0500Z 13 September], III [1900Z 16 September], IV [0900Z 20 September] and two for Stage II [0500Z 14 September and 0100Z 15 September]). Figure 8 shows the spatial distribution of water level difference between the control run (a through e) and sensitivity experiments (f through t) at each time point. Along-channel distributions of detided water level (averaged over 12 hr) at each time point are shown in Figure 9. The results from four experiments are plotted in different colors and dashed blue curves represent the linear combination
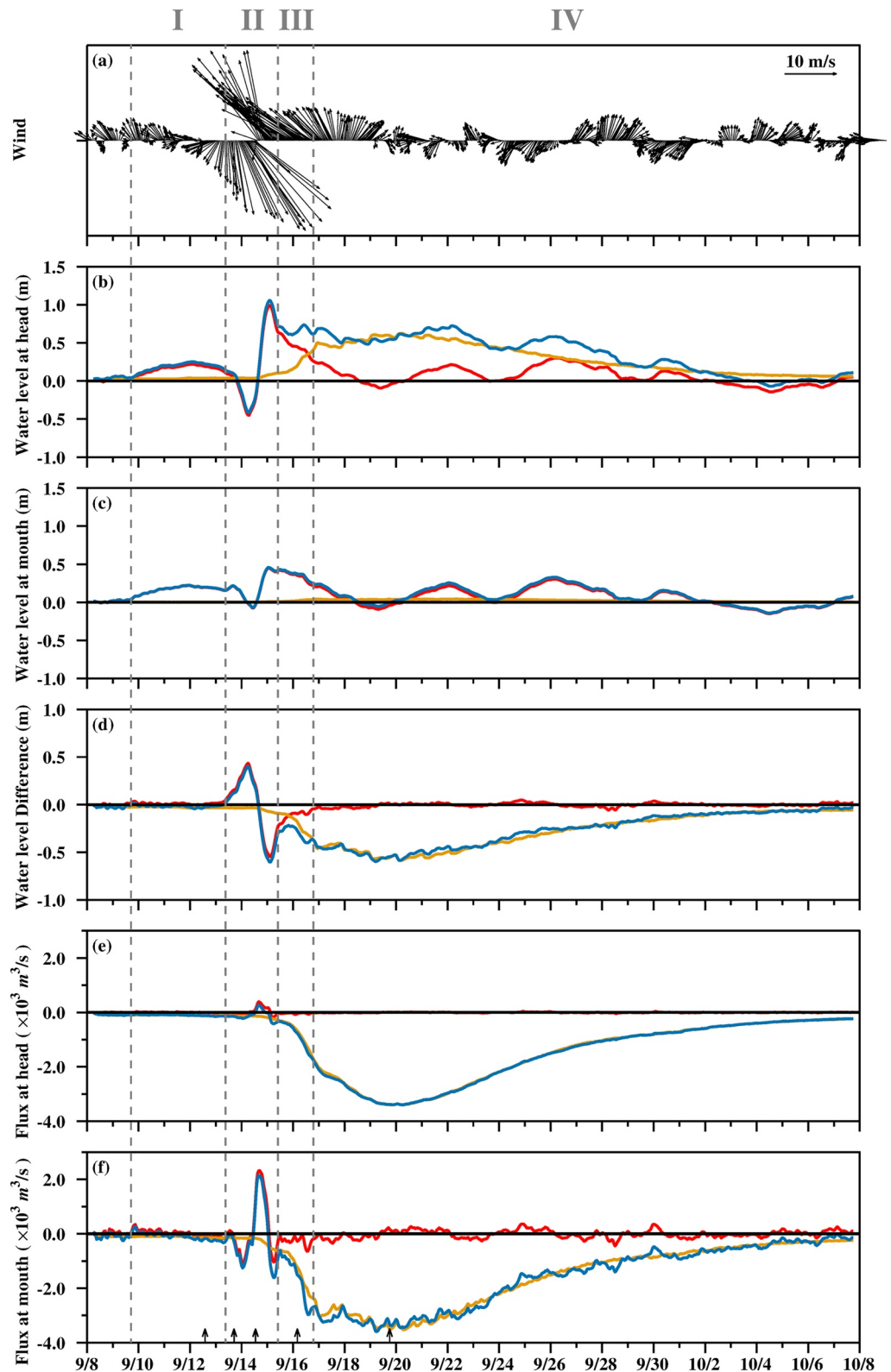
Figure 7. Time series of wind vector in the estuary (a), the water level at the estuary head (b; tr1), the water level at the mouth (c; tr2), water level difference between head and mouth (d), the flux at the head (e), and flux at the mouth (f) from Exp3 (blue), Exp4 (yellow) and Exp5 (red). Positive values in (d) indicate a southward (seaward) increasing gradient. Positive values in (e) and (f) indicate northward (landward) flux. The locations of transects are shown in Figure 3d.
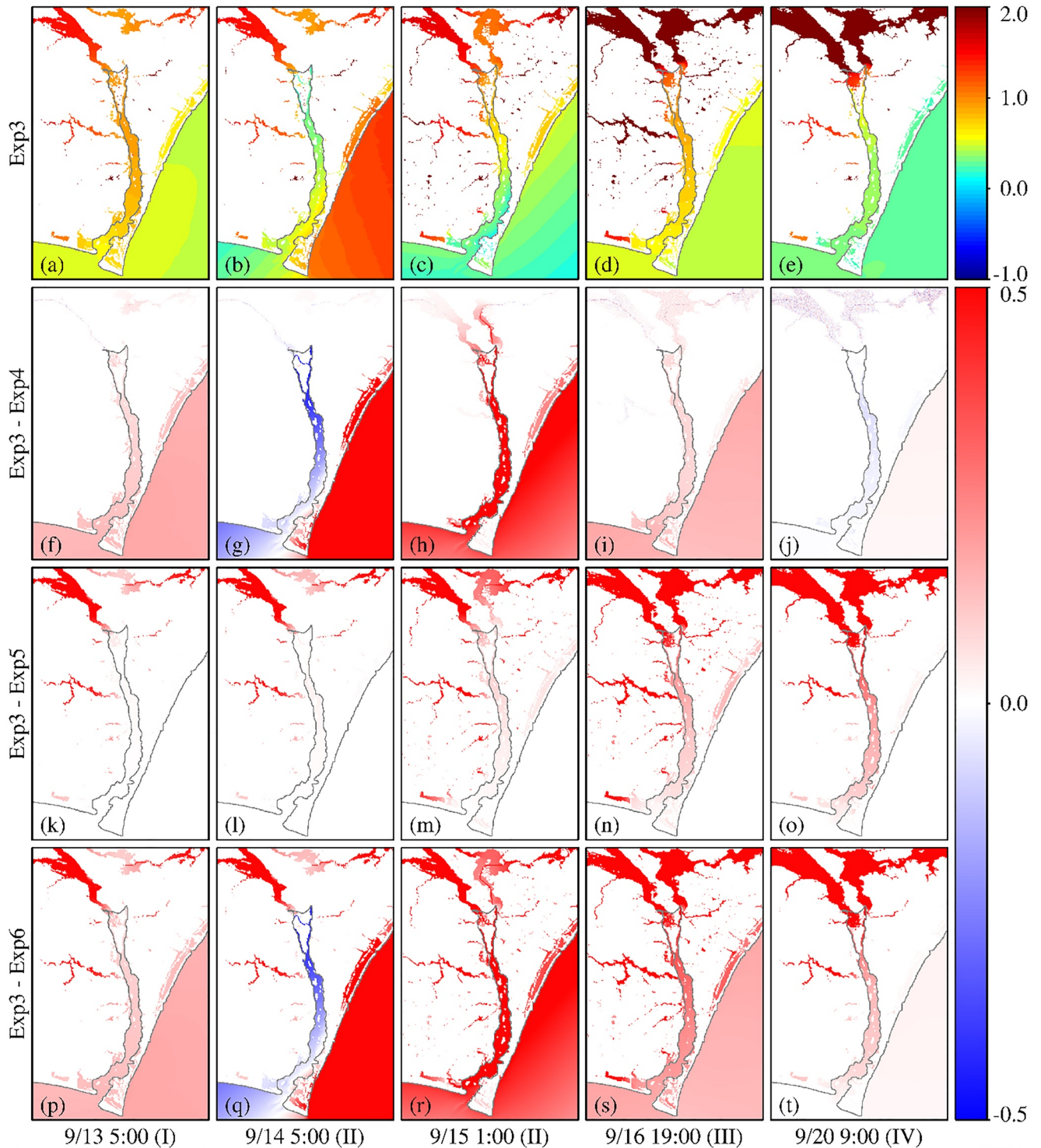
Figure 8. Water levels of control run (Exp3, a through e) and water level differences between control run and sensitivity experiments (control run minus sensitivity experiment, f through j for Exp4, k through o for Exp5, and p through t for Exp6) at the five time points throughout the simulations (arrows in Figure 7f).

of fluvial (overland runoff) and oceanic contributions (referred to hereafter as LCFO), which is calculated as (WL4 + WL5 − WL6), where WL4, WL5, and WL6 are water levels generated by Exp4, Exp5, and Exp6, respectively.
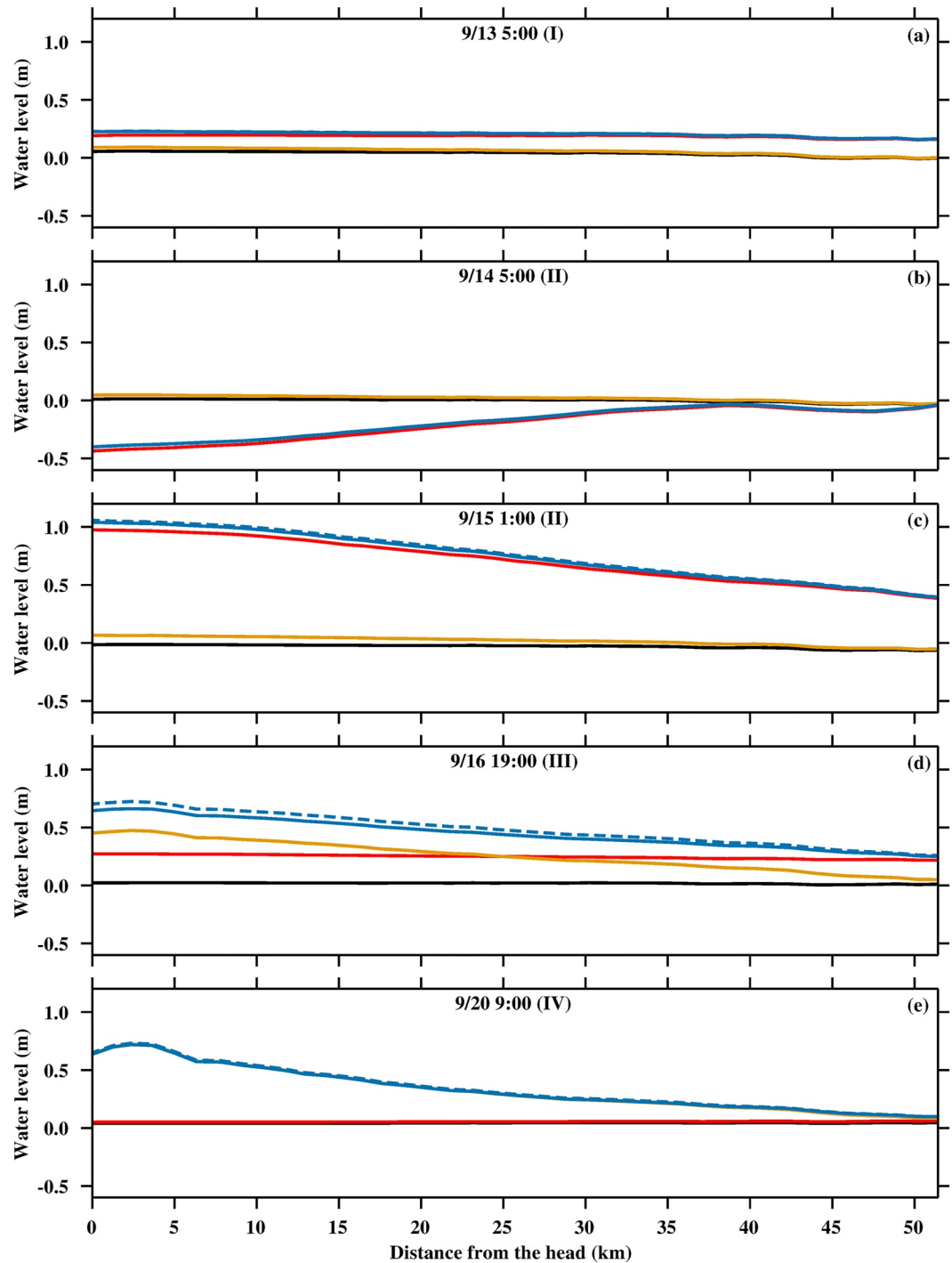
Figure 9. Along-channel distributions of detided water level from Exp3 (blue), Exp4 (yellow), Exp5 (red), Exp6 (black), and a linear combination of fluvial and oceanic contributions (dashed blue) at five time points throughout the simulations (arrows in Figure 7f, labeled in top of each panel). The along-channel sample points are shown in Figure 3d.

Stage I was from 1700Z 9 September to 0900Z 13 September. During this stage, Florence moved from ~2,200 km to less than 250 km away from the estuary (Stewart & Berg, 2019). The local wind was less than 7 m/s and did not have a fixed direction (Figure 7a). However, the remote winds were generating swell that propagated to the estuary mouth and the estuary water level was increased by 0.2 m (Figures 7b and 7c), and no surface slope was simulated (Figures 7d and 8p). The fluxes at the head and mouth were relatively small, less than 300 m³/s.

Figure 9a indicates that overland runoff increased the water level at the estuary head by 0.04 m and had no effect at the mouth. And there was no salient difference between Exp3 and LCFO.

Stage II was from 0900Z 13 September to 1000Z 15 September when Florence reached the estuary. This stage could be further divided into two substages that were both dominated by the intense local wind. The first substage was dominated by the cyclonically forced northerly wind. Strong wind-induced seaward flux at the estuary mouth (Figure 7f) was simulated. The overall water level was decreased and the water level decrease at the estuary head was more significant than that at the mouth, thus a seaward gradient was formed, with increasing water level toward the mouth (Figures 7b–7d, Figures 8g and 9b). The contribution of the surface runoff to the water level was 0.04 m at the head (Figure 9b). No salient difference was found between Exp3 and LCFO. In the second substage, a strong southerly wind was induced by the tropical cyclone moving westward. Fluxes at both the head and mouth turned northward (Figures 7e and 7f). The flux at the mouth was much larger than that at the head, resulting in a wind-forced storm surge. Water levels at both the head and mouth increased and the direction of the water-surface tilt changed from seaward to landward (Figures 7b–7d). At this substage, the wind-forced storm surge dominated the estuary and even propagated further upstream (Figure 8h). At the same time, overland runoff began to flow into the estuary (yellow curves in Figure 7). Water from Florence-induced precipitation reached the estuary and increased the water level at the head and mouth by 0.08 and 0.01 m, respectively (Figures 8m and 9c). Compared with LCFO, the water level at the head of the estuary under the compound effect of overland runoff and storm surge was reduced by 0.02 m (Exp3 vs. control run).

Stage III was defined as the period of 1000Z 15 September to 1900Z 16 September. In this stage, the wind became weaker while overland runoff became stronger compared with the previous two stages. Fluxes induced by local wind decreased at both estuary head and mouth (red curves in Figures 7e and 7f) while fluxes induced by overland runoff increased (yellow curves in Figures 7e and 7f). At the estuary head, the water level of Exp5 dropped due to the retreat of storm surge, that of Exp4 rose up because of the increasing overland runoff, thus that of Exp3 remained high under both effects (Figure 7b). At the estuary mouth, the impact of runoff was relatively limited compared with the rest of the estuary (yellow curve in Figure 7c). The water level gradient generated by Exp3 started to diverge from that of Exp5 and trend closer to that of Exp4, indicating a transition from a local-wind-dominated stage to an overland-runoff-dominated one (Figure 7d). In this stage, the water level increase that remained from the storm surge was homogeneous in the estuary due to the lack of local forcing (Figure 8i). At the same time, runoff from precipitation increased the water level by 0.4 m at the head and 0.04 m at the mouth, which is comparable with the wind effect (Figure 9d). At this moment, the estuary was under the compound effect from both fluvial and oceanic forcing. From the head to mid-estuary, the contribution of the runoff was greater, while from mid-estuary to mouth, the ocean had the larger contribution. The water level at the head from Exp3 is 0.06 m lower than the LCFO.

Stage IV began at 1900z of 16 September. At this stage, as Florence was weaker, the water level at the head was dominated by runoff with some fluctuations due to swell (Figure 7b). The water level at the mouth was not affected by strong runoff (Figure 7c). The water level gradient in Exp5 was around zero, which indicates that the water level fluctuations were not caused by a local effect (Figure 7d). The water level gradient and flux curves of Exp3 and Exp4 are similar, indicating that the estuary was dominated by runoff (Figures 7d–7f). A huge amount of water from precipitation flowed into the estuary (Figure 8e). The runoff-induced water level increase was 0.6 m at the head and 0.04 at the mouth (Figure 9e). To balance the larger drag force induced by an increased seaward velocity, a water level gradient of 0.01 m/km toward the head was generated. The water level difference at the head between Exp3 and LCFO was 0.013 m.

When local forcing is included, the water level in the estuary generates a gradient to balance the surplus forcing. In Stage II, a strong landward wind stress force was balanced by seaward pressure gradient force. The flux at the head was limited, and the effect of storm surge on the upstream region was largely reduced. In Stage IV, the enhanced drag force was balanced by a seaward pressure gradient force. The fluxes at the head and mouth remained equal; all of the water from upstream flowed into the ocean and no water was trapped in the estuary. Therefore, the estuary acts as a buffer between the potential sharp water level increase induced from ocean processes on one end, and overland runoff on the other.
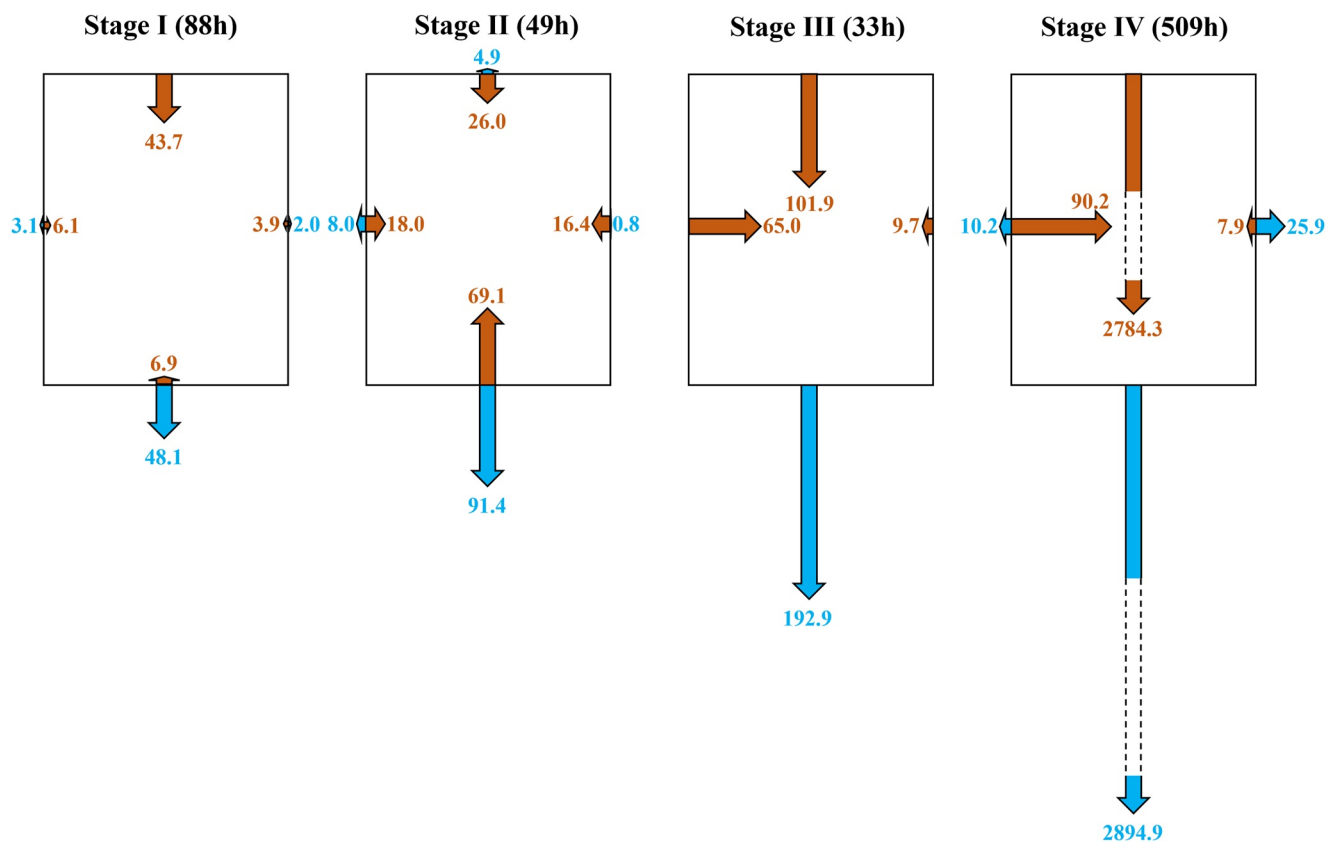
Figure 10. Water volumes of the control run (Exp3) through four transects of the estuary control volume during the four stages. Water volumes of Exp6 are subtracted from the results to exclude influences from the tides. Red arrows are flux into the estuary and blue arrow stands for flux out of the estuary. Unit: million m³.

Table 2
Net Water Transports of Exp3 Through Exp5 at Four Transects Bounding the Estuary During Four Stages

		tr1	tr2	tr3	tr4	Total
Stage I	Exp3	43.7	−41.2	3.0	1.9	7.4
	Exp4	44.0	−47.7	4.6	0.1	1.0
	Exp5	−0.5	7.0	−2.0	1.4	5.9
Stage II	Exp3	21.1	−22.3	10.0	15.6	24.5
	Exp4	27.9	−46.2	16.0	2.4	0.1
	Exp5	−6.1	24.3	−6.2	12.5	24.4
Stage III	Exp3	101.9	−192.9	65.0	9.7	−16.3
	Exp4	92.3	−156.1	60.3	8.3	4.8
	Exp5	4.0	−31.2	3.4	2.2	−21.6
Stage IV	Exp3	2784.3	−2894.9	80.0	−18.0	−48.6
	Exp4	2763.6	−2862.2	74.1	−11.4	−35.9
	Exp5	2.8	−19.3	0.7	−0.4	−16.2

Note. Net water transports of Exp6 are subtracted from the results. Positive values indicate transport into the estuary control volume. Unit: million m³.

4.2. Water Budget Analysis

In this section, we treat the estuary as a "box" bounded by the transects at the estuary head (tr1), mouth (tr2), and the two interface boundaries in the east and west, respectively (tr3 and tr4) (Figure 3d). The volume of the estuary is calculated to be 299.4 million m³. The volume of water that flowed into and out of the four transects during each of the four stages of Exp3 is shown in Figure 10. Net water volume through the four transects of Exp3 to Exp5 are shown in Table 2 to untangle the compound effect in water transportation. The results of Exp6 are subtracted from that of other experiments to exclude tidal influence. During Florence, tr1 contributes the most water input from overland runoff. Besides that, creeks on the two sides of the estuary contribute lateral water input through tr3 and tr4. Tr2 is the main water outlet of the estuary.

For Exp3, during Stage I, 43.7 million m³ of water entered the estuary from upstream while 41.2 million m³ of water flowed out of the estuary through tr2 (Figure 10). The lateral water transport was small compared with along-channel transport. The net water volumes through tr1 and tr2 in Exp4 (no wind in ROMS 2D model) were 44.0 and 47.7 million m³ seaward, respectively. For Exp5 (no precipitation in WRF-Hydro) the flux flipped its direction to landward with a 0.5 and 7.0 million m³ flux at the two transects, respectively. This result indicates that the seaward transport was mainly from runoff while landward transport was induced by swell (Table 2).

During Stage II, due to strong wind-induced storm surge, water volume through tr2 was greater than that through other transects in Exp3. 69.1 million m^3 of water entered the estuary from the ocean, while 91.4 million m^3 of water flowed out of the estuary, which included the water from both storm surge and overland runoff (Figure 10). In this stage, the contribution of lateral transport from overland runoff became notable—the model simulated that 16.0/12.5 million m^3 of water entered the estuary through tr3/tr4 in Exp4/Exp5.

During Stage III, water flowed into the estuary from tr1, tr3, and tr4, and flowed out of the estuary through tr2 (Figure 10). The influxes of water through tr1, tr3, and tr4 of Exp3 were close to that of Exp4, suggesting that this water was mainly from overland runoff (Table 2). The net water volumes through tr3 of Exp3 and Exp4 were 65 and 60 million m^3, respectively, which are comparable to the net water volumes through tr1 (101.9/92.3 million m^3 in Exp3/Exp4). Tr4 also contributed 9.7 and 8.3 million m^3 of the influx in Exp3 and Exp4, respectively. Thus, in this stage, lateral transport from overland runoff played an important role in the estuary water budget. In Exp3, the water volume through tr2 was approximately twice that through tr1, which was the result of lateral transport and retreat of the surging water. For Exp5, the water volume though tr2 was much greater than that through tr1, which indicates that the surging water began to flow out of the estuary.

During Stage IV, the water volumes transported for Exp3 through tr1 and tr2 were 2784.3 and 2894.9 million m^3 seaward, respectively. The net water volume through tr3 was 80.0 million m^3 into the estuary while the net water volume through tr4 was 18.0 million m^3 out of the estuary. The water volumes transport through all four transects of Exp4 were much greater than that of Exp5, which indicates that the water flows through the estuary were mainly from the overland runoff.

The total water volume from overland runoff during the event can be approximately calculated as the sum of water input of Exp3 during Stages III and IV (water fluxes in Stages I and II were mainly controlled by oceanic forcing and negligible compared with that in Stage III and IV). The total water volume is calculated to be 3,051.1 million m^3 which is about 10 times the estuary volume, suggesting that overland runoff flushed the Cape Fear River Estuary 10 times within 23 days (Stage III and Stage IV) after Florence's landfall.

5. Discussion

5.1. Nonlinear Effect Between Runoff and Residual Water Level From the Open Ocean

In this study, our model results indicate the dynamically coupled hydrological-ocean model is more accurate than stand-alone and linked models in reproducing water level changes. Experiments using the coupled model were then used to untangle the contribution from different processes. These results show that the detided water level simulated by the coupled model (Exp3) is smaller than the linear combination of the fluvial and oceanic contributions, LCFO (Figures 9c–9e). In this section, we discuss the mechanism behind the non-linear effect between fluvial (runoff) and oceanic forcings (non-tidal residual water level from the open ocean). To estimate the contribution of nonlinearity to the residual water level variation in the estuary, the time series of along-channel water level difference between Exp3 (control run) and LCFO is shown in Figure 11, together with the water level and water flux at tr2 (same as blue curves in Figures 7c and 7f). The water level difference is calculated as (WL3 − (WL4 + WL5 − WL6)), where WL3, WL4, WL5, and WL6 are the water levels calculated in Exp3 through Exp6, respectively. A filter with a moving average window of 12 hr is applied to remove tidal contribution.

The nonlinear effects on the detided water level decrease gradually from estuary head to mouth and are stronger during Stages III and IV than Stages I and II. Comparing the map (Figure 11a) with flux curve (red curve in Figure 11b), the occurrence of nonlinear effects is corresponding to a high runoff period (area between the two vertical dashed lines in Figure 11), which indicates that intense runoff is a necessary condition for nonlinearity. Comparing the map (Figure 11a) with the water level curve (blue curve in Figure 11b), the bluish/reddish color is corresponding to the positive/negative water level, which indicates that increased/decreased water level from the ocean induces the nonlinear effect that tends to decrease/increase water level in the estuary.

To explore the mechanism of the nonlinearity, we consider the estuary as a 1D channel with fixed depth and width. In this case, the Froude number of the channel is small even with the largest overland runoff during the event (Fr ∼ 0.03 when runoff is 3,300 m^3/s). So that the inertial terms are negligible, and a balance is achieved between pressure gradient force and friction. The momentum equation is simplified as,
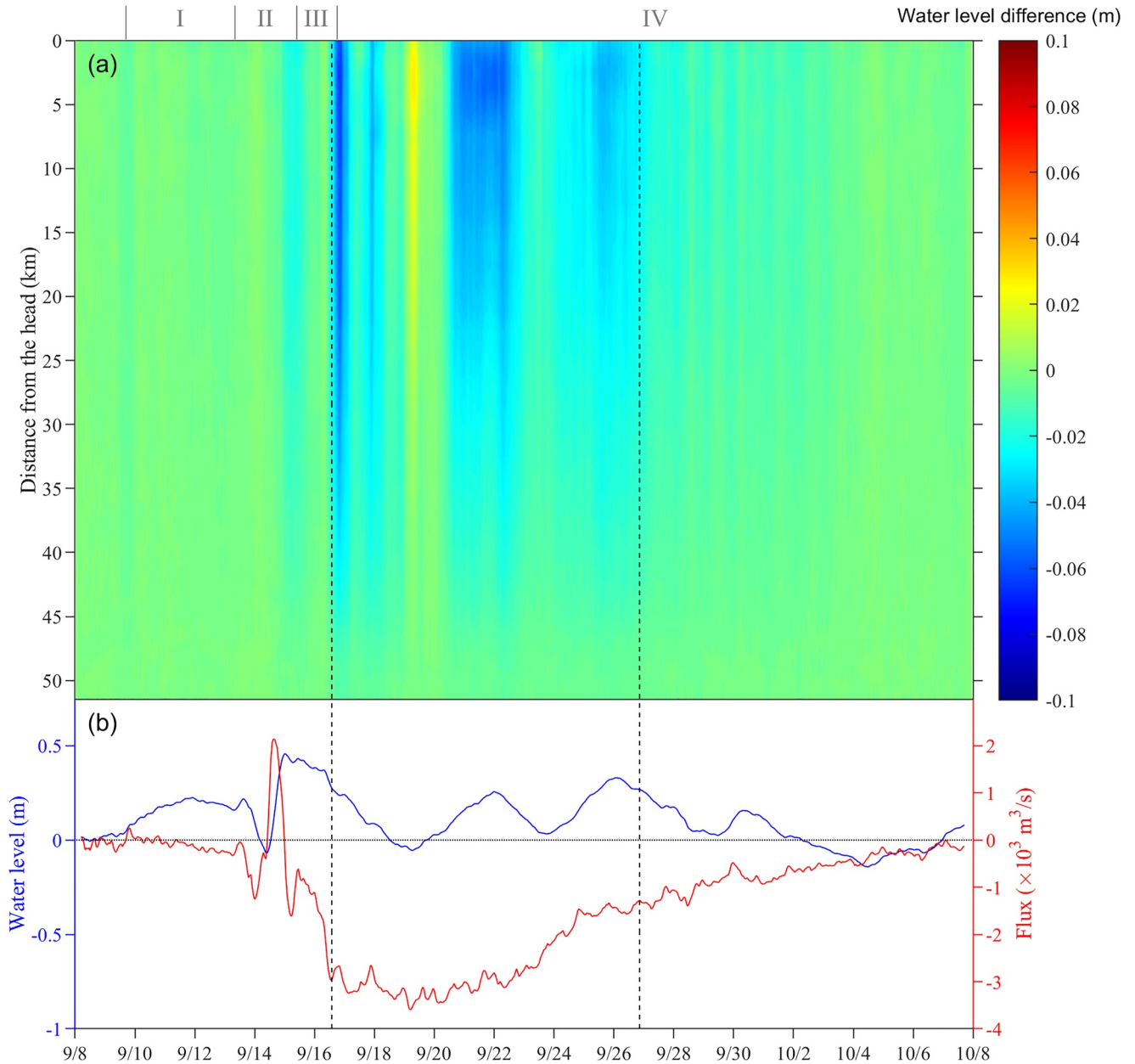
Figure 11. (a) Along-channel water level difference between the control run and the linear combination of fluvial and ocean process during the hurricane event. (b) The corresponding water level (blue) and flux (red; a positive value means northward (landward) flux) at tr2.

$$g\frac{d\eta}{dx} = C_D U^2 \tag{22}$$

where η is surface elevation, U is along-channel velocity, C_D is quadratic drag coefficient and g is the gravitational acceleration.

With given discharge from upstream, the continuity equation is simplified as,

$$Q = UW(\eta + H) \tag{23}$$

where Q is flux, W is channel width and H is water depth. Combining Equation 22 and Equation 23, the water level gradient in the channel is then,
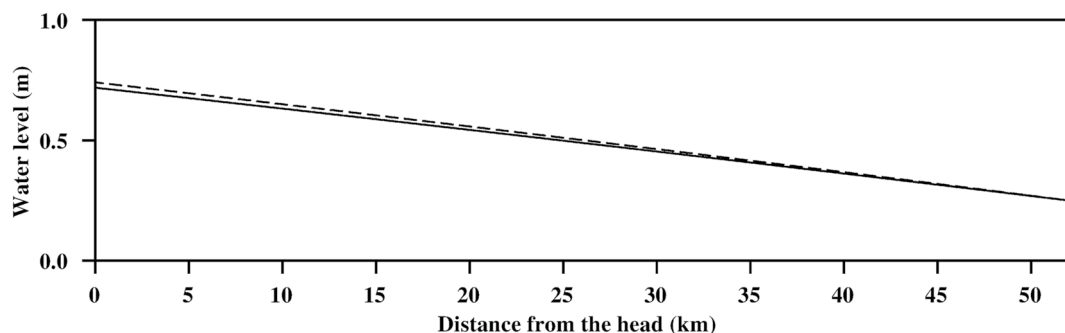
Figure 12. Water level distribution along the channel calculated from Equation 13 at 1900Z of 16 September. The solid line is the solution with $\eta_0 = 0.25$. The dashed line is the linear combination of fluvial and ocean process calculated from the solution with $\eta_0 = 0$ (runoff effect) plus a 0.25 m background value (ocean effect).

$$\frac{d\eta}{dx} = \frac{KQ^2}{(\eta + H)^2} \tag{24}$$

where $K = C_d/gW^2$.

With the boundary conditions (a) Q is given by river discharge at $x = L$ (estuary head) where L is channel length and (b) $\eta = \eta_0$ at $x = 0$ (estuary mouth) which is given by the non-tidal residual water level from the open ocean, the solution of Equation 24 is,

$$\eta = \sqrt[3]{(H + \eta_0)^3 + 3KQ^2x} - H \tag{25}$$

The estuary's depth is approximately $H = 10\,m$ and width $W = 1,000\,m$. The quadratic drag coefficient C_D is set to 3×10^{-3}. On 1900Z of 16 September when the nonlinear effect was strong, Q and η_0 were 1,800 m³/s and 0.25 m, respectively. The water level profile along the channel calculated from Equation 25 is plotted in Figure 12. The results show that the water level is around 0.7 m at the estuary head and 0.25 m at the mouth. The nonlinear effect decreases the water level at the head by 0.22 m. The theoretical model results are consistent with the coupled model results (dashed and solid blue curves in Figure 9d).

The water level difference at the estuary head ($x = L$) due to the nonlinear effect can now be derived from Equation 25 as follows

$$\Delta\eta = \sqrt[3]{(H + \eta_0)^3 + 3KLQ^2} - \sqrt[3]{H^3 + 3KLQ^2} - \eta_0 \tag{26}$$

The $\eta_0 - \Delta\eta$ plot with different Q values (Figure 13) shows that $\Delta\eta$ is negative/positive with positive/negative η_0. This suggests that an increase/decrease of water level from the ocean generates nonlinear effects that decrease/ increase the water level. This effect is due to the nonlinear expression of η_0 in Equation 25, which induces an adjustment of water level from the ocean (η_0) to the water level distribution in the estuary (η). Furthermore, the nonlinear effect increases with river flux Q getting bigger. Thus, the total residual water level in the estuary is not a direct sum of fluvial and oceanic contributions. Instead, the water level in the estuary is compounded due to the nonlinear effects between runoff and positive/negative residual water level from the open ocean, which decreases/ increases the total water level in the estuary. The nonlinear effects between fluvial and oceanic contributions indicate a buffering effect of the estuary when hurricane-induced surge happens.

5.2. Model Development Outlook

The observation-model comparisons at Wilmington station show the superior performance of the coupled model compared with the stand-alone and linked models (Section 3.3). Nevertheless, the coupled model generally underestimated the water level at Wilmington station after the landfall of Florence (after 14 September in Figure 6b). In this section, we discuss the processes that might contribute to such bias yet are not covered by this study.
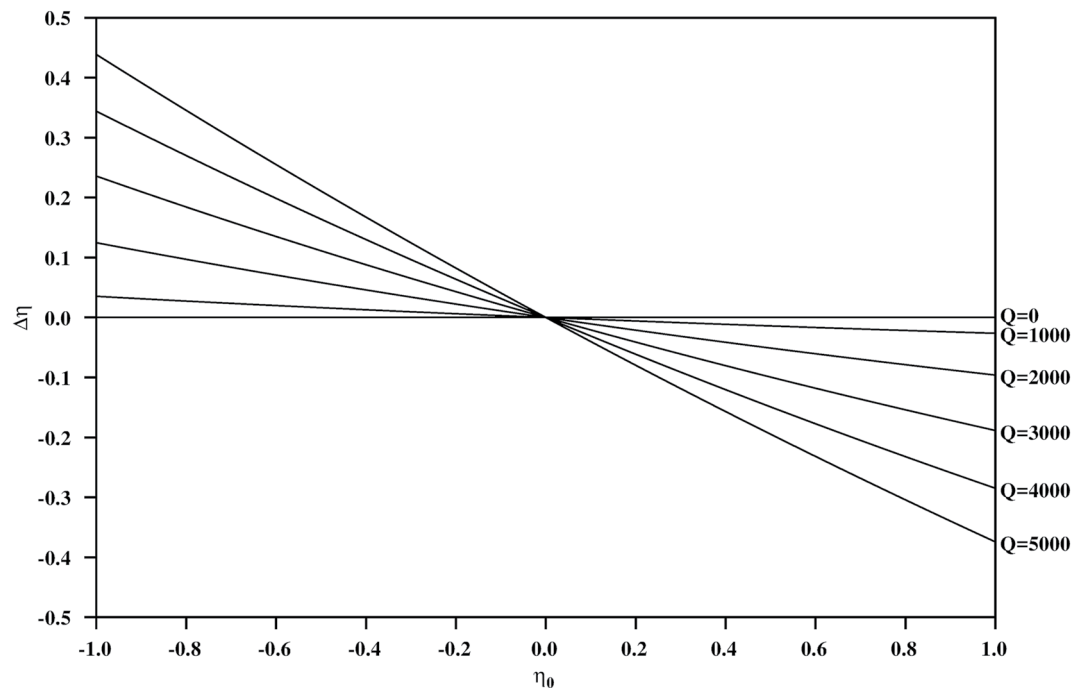
Figure 13. Correlation between detided water level from the open ocean (η_0) and nonlinear effect at estuary head ($\Delta\eta$) under different river discharge (Q).

First of all, we focus on detided water variation, and waves are not included in the model. Wave-induced setup increases the water level in coastal regions due to the dissipation of waves nearshore (Dodet et al., 2019). When interacting with storm surges, wave setup is a minor component of the total storm surge (Luo et al., 2021). However, wave setup sometimes can contribute up to 10%–35% of the total water level increase in a hurricane event (Dietrich et al., 2011, 2012; Walling et al., 2014). The total contributions from storm surges and waves are usually treated as the linear sum of both (Camus et al., 2021). Kupfer et al. (2022) present a water level increase of 45–85 cm caused by the interaction between waves and strong runoff at Breede Estuary, South Africa, which is an important flooding driver in their case. Thus, including wave has the potential to improve the underestimated water level at Wilmington station.

Our coupled model utilized the 2D barotropic version of the ROMS model. For storm surge simulations, either 2D or 3D model is adequate under proper model calibration (Zheng et al., 2013). However, the results from Ye et al. (2020) indicate that baroclinic effects can explain up to 14% of the water level error during the adjustment phase after the storm. In this study, baroclinic processes were covered by the two "parent" ROMS 3D models which provide the boundary condition for the ROMS 2D model that shares the domain with the WRF-Hydro model. The local baroclinic effects in the coupled model may not be significant due to the small computational area (maximum distance from the shoreline is 60 km) with shallow water depth (less than 35 m). However, including baroclinic effects in the coupled model still has the potential to improve the model's performance, especially during the transition stage (Stage III). Precipitation was not included in ROMS 2D model but included in the two "parent" ROMS 3D models. Since the modeled water levels at two NOAA stations matched well with observation (Figure 6), we believe that the effect of precipitation on water level variations in the relatively small computational area of ROMS 2D was not significant.

Despite the limitation in capturing certain physical processes, we see our model's potential in material exchange estimation in the land-estuary-ocean continuum as both WRF-Hydro and ROMS have a mature sediment/particle transport module (Warner et al., 2010; Yin et al., 2020). Mass flux of tracers at the interface boundary can be computed based on the water flux provided by the dynamical coupling method. With that, the coupled model can have broad applications in land-ocean exchange of the salinity, sediment, and pollutant during extreme weather events.

6. Conclusions

To investigate the compound effects of a hurricane event, a novel dynamical coupling method was developed to achieve two-way coupling between hydrological and ocean models. The two models (ROMS 2D and WRF-Hydro) exchange their water levels at the interface boundary within the modeling system COAWST. Using Hurricane Florence (2018) as a case study, the robustness of the coupled model was evaluated by comparing the model simulated water level with observations in the watershed, estuary, and along the coast. The model performed well in reproducing water level fluctuations in the river channel, estuary, and coastal ocean. The simulated water levels at the head of the Cape Fear River Estuary exhibited a 0.3–1.0 m (approximately 20%–40%) improvement during the post-hurricane period compared with the performance of the stand-alone and linked (one-way couple) ocean model.

With a series of sensitivity experiments, the contribution from different flood drivers was untangled and quantified. The compound flooding event in the Cape Fear River Estuary was categorized into four stages: (I) swelling (1700Z 19 September to 0900Z, 13 September), (II) local-wind-dominated (0900 13 September to 1000Z 15 September), (III) transition (1000Z 15 September to 1900Z 16 September) and (IV) overland-runoff-dominated (after 1900Z 16 September). In Stage I, the water level in the estuary was controlled by the wind-generated swell from the open ocean. The net water transport in the estuary was a combination of seaward transport due to overland runoff and swell-induced landward transport. In Stage II, intense local wind stress induced strong water level gradients. A huge volume of water entered the estuary due to a local wind-induced storm surge. In Stage III, the estuary was in recovery from the storm surge. At the same time, the overland runoff from hurricane-induced precipitation, including those from the west and east side of the estuary, started to enter the estuary. In Stage IV, the estuary was dominated by overland runoff. Within 23 days of Florence's landfall, the total fresh water runoff induced by Florence was calculated to be about 10 times the estuary's volume. A nonlinear effect between fluvial and oceanic processes was identified via a comparison of the water level simulated by the coupled model and that derived from the LCFO. This effect was manifested by the interaction between overland runoff and residual water level from the ocean and acted as a buffer to reduce the extreme water level changes during the event.

Data Availability Statement

WRF-Hydro (Gochis et al., 2018) is available at https://ral.ucar.edu/projects/wrf_hydro. ROMS (Shchepetkin & McWilliams, 2005) is available at https://www.myroms.org. COAWST (Warner et al., 2010) is available at https://github.com/jcwarner-usgs/COAWST. The program for model coupling is accessible at https://doi.org/10.5281/zenodo.7314817. The Zenodo link also contains all data and scripts used to generate model results shown in Figures 3–13. Availabilities of the topography, bathymetry, and forcing data used in this study are described in Section 2. The availabilities of the observed data used in this study are described in Section 3.

References

Apollonio, C., Bruno, M. F., Iemmolo, G., Molfetta, M. G., & Pellicani, R. (2020). Flood risk evaluation in ungauged coastal areas: The case study of Ippocampo (Southern Italy). *Water*, *12*(5), 1466. https://doi.org/10.3390/w12051466

Benjamin, S. G., Weygandt, S. S., Brown, J. M., Hu, M., Alexander, C. R., Smirnova, T. G., et al. (2016). A North American hourly assimilation and model forecast cycle: The Rapid Refresh. *Monthly Weather Review*, *144*(4), 1669–1694. https://doi.org/10.1175/MWR-D-15-0242.1

Bevacqua, E., Vousdoukas, M. I., Zappa, G., Hodges, K., Shepherd, T. G., Maraun, D., et al. (2020). More meteorological events that drive compound coastal flooding are projected under climate change. *Communications Earth & Environment*, *1*(1), 47. https://doi.org/10.1038/s43247-020-00044-z

Booij, N., Ris, R. C., & Holthuijsen, L. H. (1999). A third-generation wave model for coastal regions: 1. Model description and validation. *Journal of Geophysical Research*, *104*(C4), 7649–7666. https://doi.org/10.1029/98JC02622

Cai, H., Savenije, H. H. G., & Jiang, C. (2014). Analytical approach for predicting fresh water discharge in an estuary based on tidal water level observations. *Hydrology and Earth System Sciences*, *18*(10), 4153–4168. https://doi.org/10.5194/hess-18-4153-2014

Camus, P., Haigh, I. D., Nasr, A. A., Wahl, T., Darby, S. E., & Nicholls, R. J. (2021). Regional analysis of multivariate compound coastal flooding potential around Europe and environs: Sensitivity analysis and spatial patterns. *Natural Hazards and Earth System Sciences*, *21*(7), 2021–2040. https://doi.org/10.5194/nhess-21-2021-2021

Chapman, D. C. (1985). Numerical treatment of cross-shelf open boundaries in a barotropic coastal ocean model. *Journal of Physical Oceanography*, *15*(8), 1060–1075. https://doi.org/10.1175/1520-0485(1985)015<1060:NTOCSO>2.0.CO;2

Chen, C., Liu, H., & Beardsley, R. C. (2003). An unstructured grid, finite-volume, three-dimensional, primitive equations ocean model: Application to coastal ocean and estuaries. *Journal of Atmospheric and Oceanic Technology*, *20*(1), 159–186. https://doi.org/10.1175/1520-0426(2003)020<0159:AUGFVT>2.0.CO;2

Chen, M., Li, Z., Gao, S., Luo, X., Wing, O. E. J., Shen, X., et al. (2021). A comprehensive flood inundation mapping for Hurricane Harvey using an integrated hydrological and hydraulic model. *Journal of Hydrometeorology*, *22*(7), 1713–1726. https://doi.org/10.1175/JHM-D-20-0218.1

Cheng, H., Cheng, J. C., Hunter, R. M., & Lin, H. (2010). Demonstration of a Coupled Watershed-Nearshore Model. ERDC TN-SWWRP-10-2.

Cheng, J.-R. C., Cheng, H.-P., Lin, H.-C., Hunter, R. M., Richards, D. R., & Edris, E. V. (2007). Performance study of parallel algorithms in pWASH123D. In *World environmental and water resources congress 2007* (pp. 1–14). https://doi.org/10.1061/40927(243)168

Cho, K.-H., Wang, H. V., Shen, J., Valle-Levinson, A., & Teng, Y. (2012). A modeling study on the response of Chesapeake Bay to hurricane events of Floyd and Isabel. *Ocean Modelling*, *49*, 22–46. https://doi.org/10.1016/j.ocemod.2012.02.005

Colby, J. D., Mulcahy, K. A., & Wang, Y. (2001). Modeling flooding extent from Hurricane Floyd in the coastal plains of North Carolina. *Environmental Hazards*, *2*(4), 157–168. https://doi.org/10.3763/ehaz.2000.0221

Dietrich, J. C., Tanaka, S., Westerink, J. J., Dawson, C. N., Luettich, R. A., Zijlema, M., et al. (2012). Performance of the unstructured-mesh, SWAN+ADCIRC model in computing hurricane waves and surge. *Journal of Scientific Computing*, *52*(2), 468–497. https://doi.org/10.1007/s10915-011-9555-6

Dietrich, J. C., Zijlema, M., Westerink, J. J., Holthuijsen, L. H., Dawson, C., Luettich, R. A., et al. (2011). Modeling hurricane waves and storm surge using integrally-coupled, scalable computations. *Coastal Engineering*, *58*(1), 45–65. https://doi.org/10.1016/j.coastaleng.2010.08.001

Ding, Z., Zhu, J., Chen, B., & Bao, D. (2021). A two-way nesting unstructured quadrilateral grid, finite-differencing, estuarine and coastal ocean model with high-order interpolation schemes. *Journal of Marine Science and Engineering*, *9*(3), 335. https://doi.org/10.3390/jmse9030335

Dodet, G., Melet, A., Ardhuin, F., Bertin, X., Idier, D., & Almar, R. (2019). The contribution of wind-generated waves to coastal sea-level changes. *Surveys in Geophysics*, *40*(6), 1563–1601. https://doi.org/10.1007/s10712-019-09557-5

Du, J., Park, K., Dellapenna, T. M., & Clay, J. M. (2019). Dramatic hydrodynamic and sedimentary responses in Galveston Bay and adjacent inner shelf to Hurricane Harvey. *Science of the Total Environment*, *653*, 554–564. https://doi.org/10.1016/j.scitotenv.2018.10.403

Egbert, G. D., & Erofeeva, S. Y. (2002). Efficient inverse modeling of barotropic ocean tides. *Journal of Atmospheric and Oceanic Technology*, *19*(2), 183–204. https://doi.org/10.1175/1520-0426(2002)019<0183:EIMOBO>2.0.CO;2

Flather, R. A. (1987). A tidal model of the northeast Pacific. *Atmosphere-Ocean*, *25*(1), 22–45. https://doi.org/10.1080/07055900.1987.9649262

Galanaki, E., Lagouvardos, K., Kotroni, V., Giannaros, T., & Giannaros, C. (2021). Implementation of WRF-Hydro at two drainage basins in the region of Attica, Greece, for operational flood forecasting. *Natural Hazards and Earth System Sciences*, *21*(7), 1983–2000. https://doi.org/10.5194/nhess-21-1983-2021

Garvine, R. W. (1985). A simple model of estuarine subtidal fluctuations forced by local and remote wind stress. *Journal of Geophysical Research*, *90*(C6), 11945. https://doi.org/10.1029/JC090iC06p11945

Ghanbari, M., Arabi, M., Kao, S. C., Obeysekera, J., & Sweet, W. (2021). Climate change and changes in compound coastal-Riverine flooding hazard along the U.S. Coasts. *Earth's Future*, *9*(5), 1–17. https://doi.org/10.1029/2021EF002055

Gochis, D. J., Barlage, M., Dugger, A., Fitzgerald, K., Karsten, L., Mcallister, M., et al. (2018). WRF-hydro V5 technical description originally created: Updated: WRF-Hydro V5 technical description. In *NCAR technical note* (pp. 1–107).

Hill, C., DeLuca, C., BalajiSuarez, M., & Da Silva, A. (2004). The architecture of the earth system modeling framework. *Computing in Science & Engineering*, *6*(1), 18–28. https://doi.org/10.1109/MCISE.2004.1255817

Huang, W., Ye, F., Zhang, Y. J., Park, K., Du, J., Moghimi, S., et al. (2021). Compounding factors for extreme flooding around Galveston bay during hurricane Harvey. *Ocean Modelling*, *158*(November 2020), 101735. https://doi.org/10.1016/j.ocemod.2020.101735

Jacob, R., Larson, J., & Ong, E. (2005). M × N communication and parallel interpolation in community climate system model version 3 using the model coupling toolkit. *International Journal of High Performance Computing Applications*, *19*(3), 293–307. https://doi.org/10.1177/1094342005056116

Jones, P. W. (1998). A user's guide for SCRIP: A spherical coordinate remapping and interpolation package, version 1.4. Retrieved from https://www.researchgate.net/publication/258437800

Joyce, J., Chang, N.-B., Harji, R., Ruppert, T., & Singhofen, P. (2018). Cascade impact of hurricane movement, storm tidal surge, sea level rise and precipitation variability on flood assessment in a coastal urban watershed. *Climate Dynamics*, *51*(1–2), 383–409. https://doi.org/10.1007/s00382-017-3930-4

Koenig, T. A., Bruce, J. L., O'Connor, J., McGee, B. D., Holmes, R. R., Hollins, R. J., et al. (2016). Identifying and preserving high-water mark data. In *U.S Geological Survey, U.S Government Printing Office, chapter 24 of section A, surface-water techniques book 3, applications of hydraulics.*

Kumbier, K., Carvalho, R. C., Vafeidis, A. T., & Woodroffe, C. D. (2018). Investigating compound flooding in an estuary using hydrodynamic modelling: A case study from the Shoalhaven River, Australia. *Natural Hazards and Earth System Sciences*, *18*(2), 463–477. https://doi.org/10.5194/nhess-18-463-2018

Kupfer, S., Santamaria-Aguilar, S., van Niekerk, L., Lück-Vogel, M., & Vafeidis, A. T. (2022). Investigating the interaction of waves and river discharge during compound flooding at Breede Estuary, South Africa. *Natural Hazards and Earth System Sciences*, *22*(1), 187–205. https://doi.org/10.5194/nhess-22-187-2022

Li, M., Zhong, L., Boicourt, W. C., Zhang, S., & Zhang, D. L. (2006). Hurricane-induced storm surges, currents and destratification in a semi-enclosed bay. *Geophysical Research Letters*, *33*(2), 20–23. https://doi.org/10.1029/2005GL024992

Luettich, R. A., Westerink, J., & Scheffner, N. (1992). ADCIRC: An advanced three-dimensional circulation model for Shelves, coasts, and estuaries. Report 1. Theory and methodology of ADCIRC-2DDI and ADCIRC-3DL. In *Dredging research program technical report DRP-92-6* (p. 143).

Luo, Z., Huang, B., Chen, X., Tan, C., Qiu, J., & Huang, G. (2021). Effects of wave–current interaction on storm surge in the Pearl River Estuary: A case study of super typhoon Mangkhut. *Frontiers in Marine Science*, *8*, 1037. https://doi.org/10.3389/fmars.2021.692359

Majidzadeh, H., Uzun, H., Ruecker, A., Miller, D., Vernon, J., Zhang, H., et al. (2017). Extreme flooding mobilized dissolved organic matter from coastal forested wetlands. *Biogeochemistry*, *136*(3), 293–309. https://doi.org/10.1007/s10533-017-0394-x

Miles, T., Seroka, G., & Glenn, S. (2017). Coastal ocean circulation during Hurricane Sandy. *Journal of Geophysical Research: Oceans*, *122*(9), 7095–7114. https://doi.org/10.1002/2017JC013031

Moftakhari, H. R., Salvadori, G., AghaKouchak, A., Sanders, B. F., & Matthew, R. A. (2017). Compounding effects of sea level rise and fluvial flooding. *Proceedings of the National Academy of Sciences of the United States of America*, *114*(37), 9785–9790. https://doi.org/10.1073/pnas.1620325114

Muñoz, D. F., Moftakhari, H., & Moradkhani, H. (2020). Compound effects of flood drivers and wetland elevation correction on coastal flood hazard assessment. *Water Resources Research*, *56*(7), e2020WR027544. https://doi.org/10.1029/2020WR027544

Niu, G.-Y., Yang, Z.-L., Mitchell, K. E., Chen, F., Ek, M. B., Barlage, M., et al. (2011). The community Noah land surface model with multiparameterization options (Noah-MP): 1. Model description and evaluation with local-scale measurements. *Journal of Geophysical Research*, *116*(D12), D12109. https://doi.org/10.1029/2010JD015139

Noh, S., Lee, J.-H., Lee, S., & Seo, D.-J. (2019). Retrospective dynamic inundation mapping of Hurricane Harvey flooding in the Houston metropolitan area using high-resolution modeling and high-performance computing. *Water*, *11*(3), 597. https://doi.org/10.3390/w11030597

Olabarrieta, M., Warner, J. C., Armstrong, B., Zambon, J. B., & He, R. (2012). Ocean-atmosphere dynamics during Hurricane Ida and Nor'Ida: An application of the coupled ocean-atmosphere-wave-sediment transport (COAWST) modeling system. *Ocean Modelling*, *43*, 112–137. https://doi.org/10.1016/j.ocemod.2011.12.008

Pal, S., Dominguez, F., Dillon, M. E., Alvarez, J., Garcia, C. M., Nesbitt, S. W., & Gochis, D. (2021). Hydrometeorological observations and modeling of an extreme rainfall event using WRF and WRF-hydro during the RELAMPAGO field campaign in Argentina. *Journal of Hydrometeorology*, *22*(2), 331–351. https://doi.org/10.1175/JHM-D-20-0133.1

Pasquier, U., He, Y., Hooton, S., Goulden, M., & Hiscock, K. M. (2019). An integrated 1D–2D hydraulic modelling approach to assess the sensitivity of a coastal region to compound flooding hazard under climate change. *Natural Hazards*, *98*(3), 915–937. https://doi.org/10.1007/s11069-018-3462-1

Perdikaris, J., Gharabaghi, B., & Rudra, R. (2018). Evaluation of the simplified dynamic wave, diffusion wave and the full dynamic wave flood routing models. *Earth Science Research*, *7*(2), 14. https://doi.org/10.5539/esr.v7n2p14

Pietrafesa, L., Zhang, H., Bao, S., Gayes, P., & Hallstrom, J. (2019). Coastal flooding and inundation and inland flooding due to downstream blocking. *Journal of Marine Science and Engineering*, *7*(10), 336. https://doi.org/10.3390/jmse7100336

Rego, J. L., & Li, C. (2010). Nonlinear terms in storm surge predictions: Effect of tide and shelf geometry with case study from Hurricane Rita. *Journal of Geophysical Research*, *115*(C6), C06020. https://doi.org/10.1029/2009JC005285

Ryu, Y., Lim, Y. J., Ji, H. S., Park, H. H., Chang, E. C., & Kim, B. J. (2017). Applying a coupled hydrometeorological simulation system to flash flood forecasting over the Korean Peninsula. *Asia-Pacific Journal of Atmospheric Sciences*, *53*(4), 421–430. https://doi.org/10.1007/s13143-017-0045-0

Santiago-Collazo, F. L., Bilskie, M. V., & Hagen, S. C. (2019). A comprehensive review of compound inundation models in low-gradient coastal watersheds. *Environmental Modelling & Software*, *119*(June), 166–181. https://doi.org/10.1016/j.envsoft.2019.06.002

Shchepetkin, A. F., & McWilliams, J. C. (2005). The regional oceanic modeling system (ROMS): A split-explicit, free-surface, topography-following-coordinate oceanic model. *Ocean Modelling*, *9*(4), 347–404. https://doi.org/10.1016/j.ocemod.2004.08.002

Skamarock, W. C., Klemp, J. B., Dudhia, J., Gill, D. O., Liu, Z., Berner, J., et al. (2021). A description of the advanced research WRF model version 4.3. In *NCAR technical note NCAR/TN-556+STR*. https://doi.org/10.5065/1dfh-6p97

Steffen, J., & Bourassa, M. (2020). Upper-ocean response to precipitation forcing in an ocean model hindcast of hurricane Gonzalo. *Journal of Physical Oceanography*, *50*(11), 3219–3234. https://doi.org/10.1175/JPO-D-19-0277.1

Stewart, S. R., & Berg, R. (2019). *National Hurricane Center Tropical Cyclone Report: Hurricane Florence (AL062018)* (pp. 1–98). National Hurricane Center.

Tang, H. S., Chien, S. I. J., Temimi, M., Blain, C. A., Ke, Q., Zhao, L., & Kraatz, S. (2013). Vulnerability of population and transportation infrastructure at the east bank of Delaware Bay due to coastal flooding in sea-level rise conditions. *Natural Hazards*, *69*(1), 141–163. https://doi.org/10.1007/s11069-013-0691-1

Tang, H. S., Kraatz, S., Wu, X. G., Cheng, W. L., Qu, K., & Polly, J. (2013). Coupling of shallow water and circulation models for prediction of multiphysics coastal flows: Method, implementation, and experiment. *Ocean Engineering*, *62*, 56–67. https://doi.org/10.1016/j.oceaneng.2012.12.050

Valle-Levinson, A., Olabarrieta, M., & Heilman, L. (2020). Compound flooding in Houston-Galveston Bay during Hurricane Harvey. *Science of the Total Environment*, *747*, 141272. https://doi.org/10.1016/j.scitotenv.2020.141272

Wahl, T., Jain, S., Bender, J., Meyers, S. D., & Luther, M. E. (2015). Increasing risk of compound flooding from storm surge and rainfall for major US cities. *Nature Climate Change*, *5*(12), 1093–1097. https://doi.org/10.1038/nclimate2736

Walling, K., Miller, J. K., Herrington, T., & Eble, A. (2014). Comparison of Hurricane Sandy impacts in three New Jersey coastal communities. *Coastal Engineering Proceedings*, *1*(34), 38. https://doi.org/10.9753/icce.v34.management.38

Warner, J. C., Armstrong, B., He, R., & Zambon, J. B. (2010). Development of a Coupled Ocean-Atmosphere-Wave-sediment transport (COAWST) modeling system. *Ocean Modelling*, *35*(3), 230–244. https://doi.org/10.1016/j.ocemod.2010.07.010

Wehbe, Y., Temimi, M., Weston, M., Chaouch, N., Branch, O., Schwitalla, T., et al. (2019). Analysis of an extreme weather event in a hyper-arid region using WRF-Hydro coupling, station, and satellite data. *Natural Hazards and Earth System Sciences*, *19*(6), 1129–1149. https://doi.org/10.5194/nhess-19-1129-2019

Wigmosta, M. S., & Lettenmaier, D. P. (1999). A comparison of simplified methods for routing topographically driven subsurface flow. *Water Resources Research*, *35*(1), 255–264. https://doi.org/10.1029/1998WR900017

Wigmosta, M. S., Vail, L. W., & Lettenmaier, D. P. (1994). A distributed hydrology-vegetation model for complex terrain. *Water Resources Research*, *30*(6), 1665–1679. https://doi.org/10.1029/94WR00436

Winsemius, H. C., Aerts, J. C. J. H., Van Beek, L. P. H., Bierkens, M. F. P., Bouwman, A., Jongman, B., et al. (2016). Global drivers of future river flood risk. *Nature Climate Change*, *6*(4), 381–385. https://doi.org/10.1038/nclimate2893

Ye, F., Huang, W., Zhang, Y. J., Moghimi, S., Myers, E., Pe'eri, S., & Yu, H. C. (2021). A cross-scale study for compound flooding processes during Hurricane Florence. *Natural Hazards and Earth System Sciences*, *21*(6), 1703–1719. https://doi.org/10.5194/nhess-21-1703-2021

Ye, F., Zhang, Y. J., Yu, H., Sun, W., Moghimi, S., Myers, E., et al. (2020). Simulating storm surge and compound flooding events with a creek-to-ocean model: Importance of baroclinic effects. *Ocean Modelling*, *145*(July 2019), 101526. https://doi.org/10.1016/j.ocemod.2019.101526

Yin, D., Xue, Z., Gochis, D. J., Yu, W., Morales, M., & Rafieeinasab, A. (2020). A process-based, fully distributed soil erosion and sediment transport model for WRF-hydro. *Water*, *12*(6), 1840. https://doi.org/10.3390/w12061840

Yin, D., Xue, Z. G., Bao, D., RafieeiNasab, A., Huang, Y., Morales, M., & Warner, J. C. (2022). Understanding the role of initial soil moisture and precipitation magnitude in flood forecast using a hydrometeorological modeling system. *Hydrological Processes*, *36*(10), e14710. https://doi.org/10.1002/hyp.14710

Yin, D., Xue, Z. G., Warner, J. C., Bao, D., Huang, Y., & Yu, W. (2021). Hydrometeorology and hydrology of flooding in Cape Fear River basin during hurricane Florence in 2018. *Journal of Hydrology*, *603*, 127139. https://doi.org/10.1016/j.jhydrol.2021.127139

Yin, J., Lin, N., & Yu, D. (2016). Coupled modeling of storm surge and coastal inundation: A case study in New York city during Hurricane Sandy. *Water Resources Research*, *52*(11), 8685–8699. https://doi.org/10.1002/2016WR019102

Zambon, J. B., He, R., & Warner, J. C. (2014a). Investigation of Hurricane Ivan using the coupled ocean–atmosphere–wave–sediment transport (COAWST) model. *Ocean Dynamics*, *64*(11), 1535–1554. https://doi.org/10.1007/s10236-014-0777-7

Zambon, J. B., He, R., & Warner, J. C. (2014b). Tropical to extratropical: Marine environmental changes associated with Superstorm Sandy prior to its landfall. *Geophysical Research Letters*, *41*(24), 8935–8943. https://doi.org/10.1002/2014GL061357

Zambon, J. B., He, R., Warner, J. C., & Hegermiller, C. A. (2021). Impact of SST and surface waves on Hurricane Florence (2018): A coupled modeling investigation. *Weather and Forecasting*, *36*(5), 1713–1734. https://doi.org/10.1175/WAF-D-20-0171.1

Zang, Z., Xue, Z. G., Bao, S., Chen, Q., Walker, N. D., Haag, A. S., et al. (2018). Numerical study of sediment dynamics during Hurricane Gustav. *Ocean Modelling*, *126*(April), 29–42. https://doi.org/10.1016/j.ocemod.2018.04.002

Zhang, Y. J., Ye, F., Yu, H., Sun, W., Moghimi, S., Myers, E., et al. (2020). Simulating compound flooding events in a hurricane. *Ocean Dynamics*, *70*(5), 621–640. https://doi.org/10.1007/s10236-020-01351-x

Zheng, L., Weisberg, R. H., Huang, Y., Luettich, R. A., Westerink, J. J., Kerr, P. C., et al. (2013). Implications from the comparisons between two- and three-dimensional model simulations of the Hurricane Ike storm surge. *Journal of Geophysical Research: Oceans*, *118*(7), 3350–3369. https://doi.org/10.1002/jgrc.20248